COPRIME AND NESTED ARRAY PROCESSING OF THE ELBA ISLAND SONAR DATA SET

by

Vaibhav Chavali

A Thesis
Submitted to the
Graduate Faculty
of
George Mason University
In Partial fulfillment of
The Requirements for the Degree
of
Master of Science
Electrical Engineering

Committee:

_____	Dr. Kathleen E. Wage, Thesis Director
_____	Dr. Jill K. Nelson, Committee Member
_____	Dr. Zhi Tian, Committee Member
_____	Dr. Monson H. Hayes, Chair, Department of Electrical and Computer Engineering
_____	Dr. Kenneth S. Ball, Dean, Volgenau School of Engineering

Date: _____ Spring Semester 2017
George Mason University
Fairfax, VA

Coprime and Nested Array Processing of the Elba Island Sonar Data Set

A thesis submitted in partial fulfillment of the requirements for the degree of Master of Science at George Mason University

By

Vaibhav Chavali
Bachelor of Science
University of Mumbai, 2012

Director: Dr. Kathleen E. Wage, Professor
Department of Electrical and Computer Engineering

Spring Semester 2017
George Mason University
Fairfax, VA

Dedication

I dedicate this thesis to my family, friends, professors and mentors for always being there for me.

Acknowledgments

Firstly, I would like to thank my advisor, Prof. Kathleen Wage, for letting me work on this research project. Prof. Wage has guided me for the past 4 years sharing her immense knowledge in the field signal processing. Thanks also to Dr. John Buck for many useful technical discussions regarding this research.

My experiences as a teaching assistant has taught me how important it is to learn by teaching and learn through mistakes. Thanks again to my advisor Prof. Wage for suggesting different methods to improve my teaching skills. Thanks to Prof. Jill Nelson, Prof. Monson Hayes and Prof. Llyod Griffiths for letting me assist them in teaching signal processing courses at Volgenau school of engineering.

I would also like to thank my fellow researchers Srikanth Tenneti, Chun-Lin Liu, Kaushallya Adhikari, Yang Liu, Ray Bautista and Juan Ramirez for sharing their insights on improving my work and presentation skils. My colleagues in the Ocean Acoustic Signal Processing Group have helped me get to where I am and I will always be indebted to their support and encouragement. Thanks to Mehdi Farrokhrooz, Marjan Saadati, Negar Etemadyrad, Sai Kashyap and Phi Nguyen.

I can not imagine being in this position without being grateful to my friends: Aditya Harikrishnan, Trilake Nath Singh, Amrita Banerjee, Vignesh Gouthaman, Vishal Shah, Kunal Pillai, Taylor Smith, Gerard Johnston, Aneri Sanghavi, Bravim Chavan, Rushil Patel, Kartik Santhanam, Gautam Shankar, Pawan Kumar Gullapalli, Sumit Kawatra, Brijesh Salian, Nishit Babaria, Chris Walker, Leo Taffe, Soumyadeep Ghoshal, Anubha Swami, Anisha Kamble, Ambar Choudhary, Ajit CR, Shashank Nautiyal, Akshay Muralidhar, Saumitra Nagle and Divya Hegde.

Finally, I can not end without acknowledging the love and support from my family. My parents Dr. Prakash Chavali and Shailaja Chavali have been my idols and I can not thank them enough for raising me to be what I am today. My elder brother Adarsh Chavali and I have grown up with the same fondness for multi-disciplinary engineering subjects and have always questioned each other endlessly, I thank him for always being there for me. Last but not at all the least, Bharath Jayaram, I consider him as my second elder brother. Our love for carnatic music has been a major driving force in our lives. With a sincere note of thanks, I dedicate this thesis to everyone.

Funding for this work was provided by the Office of Naval Research Basic Research Challenge Program through award N00014-13-1-0229.

Table of Contents

List of Tables

List of Figures

Abstract

COPRIME AND NESTED ARRAY PROCESSING OF THE ELBA ISLAND SONAR DATA SET

Vaibhav Chavali

George Mason University, 2017

Thesis Director: Dr. Kathleen E. Wage

Sensor arrays can provide estimates of the spatial spectrum associated with propagating waves in a variety of environments, e.g., acoustic waves in the ocean. Vaidyanathan and Pal [IEEE Trans. Sig. Proc., 2010, 2011] describe coprime and nested array geometries that provide significant sensor savings when compared to densely populated Uniform Linear Arrays (ULAs). Coprime Sensor Arrays (CSAs) and Nested Arrays (NAs) consist of two interleaved subarrays with different sample spacings. To reduce the number of sensors, at least one of the subarrays is undersampled. There are several approaches to estimating the spatial power spectrum given a sparse set of CSA or NA measurements. The classical approach is to implement a multiplicative processor. Multiplication of the beamformed outputs of two undersampled subarrays eliminates the ambiguity due to aliasing, but requires temporal averaging to mitigate cross terms. This approach relies on the assumption that signals arriving from different directions are uncorrelated. Recently Liu and Buck proposed an alternative that is not restricted to uncorrelated signals [IEEE SAM, 2016]. Their min processor uses the minimum of the two subarray outputs as the spectral estimate.

The goal of this thesis is to design and implement CSA and NA processing for data from an underwater vertical line array deployed near Elba Island. Building on the work of Adhikari et al. [EURASIP J. Advances Sig. Proc., 2014], this thesis shows that CSA and NA designs for the Elba experiment can attain beampatterns comparable to a fully populated ULA using 33% fewer sensors. As noted above, one drawback of the standard multiplicative processing approach is the need for time averaging to reduce cross terms. Prior work has not quantified the amount of averaging required. This thesis analyzes cross terms using a Gaussian signal model and shows that they decay at a rate of 5 dB per decade of snapshots averaged. Finally, this thesis implements CSA and NA multiplicative and min processing for the Elba data set. Compared to the conventional spectrum obtained with the ULA, the multiplicative CSA and NA spectra for the Elba data contain endfire interference due to cross terms associated with coherent mode arrivals. Liu and Buck's min processor applied to the NA design performs the best for the Elba data set.

Chapter 1: Introduction

1.1 Motivation

The human auditory system is a naturally occurring example of a sensor array. This two sensor array receives acoustic radiation and by processing the received sound it can obtain directional information about the source. In signal processing, this basic concept has been able to provide with the ability to process propagating waves using an array of sensors/transducers. By combining the outputs of individual sensors intelligently, the user can gather information about the propagating signals in a given spatial field, e.g., identifying the source of the propagating signals, characterizing the location of the source with respect to the array, tracking certain moving sources in space, enhancing certain aspects of the signal, etc. Array signal processing applications are common in the fields of radar, radio astronomy, sonar, communications, direction finding, seismology and medical diagnosis and treatment [1, 2].

Applications require a variety of array geometries, e.g., linear (1-D), planar (2-D), and volumetric (3-D). This thesis focuses on linear array geometries where all the sensors are placed along a line. The spacing between sensors may be *uniform* or *non-uniform*. Figure 1.1 illustrates an 11-element Uniform Linear Array (ULA) with intersensor spacing d. The wavefront incident on the sensor array propagating from a source located far from the array can be idealized as a plane wave.

Plane wave signals received at the individual sensor positions of the ULA are delayed relative to a reference (zero delay) sensor position. The angle of incidence (θ) the wavefront makes with respect to the axis of the array can de determined by correcting for the phase corresponding to the delay observed at the respective sensor positions using the Fourier relationship of a time delay to a change in phase in the frequency domain. This technique is

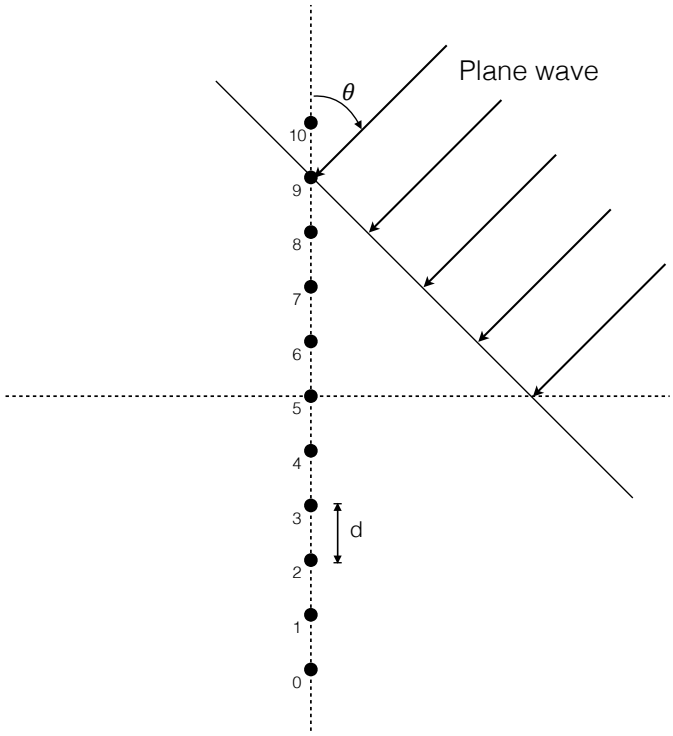

Figure 1.1: A 11-element linear array with uniform intersensor spacing d m

called *beamforming* or spatial filtering and the filter/processor that performs this operation is called a *beamformer* [1]. Analogous to sampling a time domain signal at the Nyquist frequency [3], sampling a spatial field using a ULA requires that the intersensor spacing must be less than half-wavelength of the propagating signal to avoid spatial aliasing. ULAs have been studied extensively; see the text by Van Trees [1] for a thorough bibliography.

Comparable to the frequency response of a time-domain filter, the *beampattern* is the plane-wave response of the spatial filter/beamformer [4]. An array's ability to resolve two closely spaced sources is determined by the mainlobe width of its beampattern. The resolution is inversely proportional to the width of the mainlobe. For high resolution a ULA must span a large aperture which typically requires a large number of closely spaced sensors. This thesis considers the application of sensor arrays to an underwater passive sonar experiment. Long arrays with dense spacing may be prohibitively expensive because they require large

number of sensors and a system architecture capable of high computational throughput. To reduce the number of sensors and the associated costs, a variety of alternative non-uniform array geometries have been proposed [5,6,7,8,9,10]. These non-uniform linear arrays require fewer sensors and provide similar or in some cases better resolution and peak sidelobe levels than the equally spaced linear arrays. During the late 1960s Moffet proposed one of the most attractive solutions to the non-uniform array design problem known as a Minimum Redundancy Array (MRA) [11]. Designing these non-uniform linear arrays requires extensive algorithms to search and identify the exact sensor positions that provide the desired performance [12, 13]. Moreover, these arrays were designed with the idea of estimating the covariance matrix using the lags observed in the difference co-array (virtual ULA) and then proceeding with conventional beamforming to obtain estimates of the spatial spectrum.

In the past multiplicative processors have been used widely in applications related to radio astronomy and radar. The multiplication of the array patterns of two sparse subarrays can be matched to the array pattern of a fully populated ULA [14, 15]. Shaw and Davies show that multiplicative processors are capable of providing improved resolution and low sidelobe patterns using the subarrays of a given ULA [16, 17]. The issue of cross terms was addressed by Ksienski [18] and Pedinoff [19]. They observed the presence of cross terms or cross products at the output of a multiplicative processor in multiple target/source scenarios for radar applications. Davies suggested averaging over multiple snapshots when the two targets/sources are uncorrelated to reduce their effect [20], although he did not comment on the number of snapshots needed for averaging.

Vaidyanathan and Pal proposed two such non-uniform array geometries with a clearly specified sensor arrangement, namely, coprime and nested arrays [21, 22]. These arrays use two interleaved uniform linear subarrays. Since a reduction in the number of sensors was the main incentive for these designs, at least one of the subarrays was undersampled, i.e., the intersensor spacing was greater than half-wavelength. The interleaved subarray design employed in coprime and nested arrays inspired Vaidyanathan and Pal to suggest the use of multiplicative processors to estimate a spatial spectrum. By multiplying the beamformed

output of the individual subarrays, the multiplicative processors eliminate the ambiguity due to the undersampling. More recently, Adhikari et al. showed that by adding more sensors to the subarrays, the multiplicative processors are capable of providing similar sidelobe levels as the conventional processor using a variety of array shading/tapering functions [23]. Adhikari et al.'s approach allowed for the extension of the subarrays outside the aperture of the fully populated ULA which is not practical when the array size is limited by cost or environmental constraints. Liu and Buck propose the use of a min processor, that uses the minimum of the two subarray outputs as the spectral estimate [24]. This intuitive approach is an attractive option when the signals sensed by the passive sonar is spatially bandlimited and it does not require uncorrelated sources.

1.2 Objectives

The previous section highlights some of the issues concerning the design of coprime and nested arrays that incorporate the use of multiplicative processors. This thesis presents the problem of designing coprime and nested arrays that make use of a reduced number of sensors when compared to a fixed aperture ULA used in an underwater passive sonar experiment near Elba Island. This motivates the need for a detailed analysis of the design and performance of coprime/nested multiplicative and min processors in estimating the spatial spectrum using the data received by the $48-$sensor ULA used in the Elba experiment.

The objectives of this thesis are:

- To design coprime and nested array geometries that provide similar multiplicative and min beampattern performance as the benchmark conventional ULA.
- To analyze the cross terms of a multiplicative processor using a Gaussian signal model and to derive the cross term decay as a function of snapshots.
- To implement the coprime and nested beamformers for the Elba data set and assess the performance of the multiplicative and min processors using knowledge of the acoustic propagation environment.

1.3 Contributions

Results of this thesis have been published in one conference paper and 2 conference abstracts. Two journal papers are in preparation. An invited talk will be presented at the upcoming Acoustical Society of America (ASA) meeting in June 2017.

Publications

- V. Chavali, K. E. Wage, and J. R. Buck, Coprime processing for the Elba Island sonar data set, in *IEEE 48th Asilomar Conference on Signals, Systems and Computers*, 2014, pp. 1864-1868.
- ——, Design of coprime and nested arrays to analyze the Elba Island data set using multiplicative and min processors, to be submitted to *The Journal of the Acoustical Society of America*. (Manuscript in preparation).
- V. Chavali, K. E. Wage, Cross term decay in multiplicative processors, to be submitted to *IEEE Signal Processing Letters*. (Manuscript in preparation).

Conference Abstracts

- V. Chavali, K. E. Wage, and J. R. Buck, Design of a coprime array for the North Elba sea trial, *Journal of the Acoustical Society of America*, vol. 136, no. 4, p. 2147, 2014.
- V. Chavali and K. E. Wage, Design of nested and coprime arrays for the North Elba sea trial, in *IEEE Underwater Acoustic Signal Processing Workshop*, Oct. 2015.
- ——, Comparison of multiplicative and min processors for coprime and nested geometries using the Elba Island data set, *Journal of the Acoustical Society of America*. (to be presented in June 2017).

1.4 Organization

Chapter 2 provides provides an overview of the the Elba data set using conventional ULA processing. It also reviews the coprime and nested arrays proposed by Vaidyanathan and

Pal. Chapter 3 designs coprime and nested arrays for the Elba ULA and compares the multiplicative and min beampatterns to the ULA. Chapter 4 formulates the problem of cross term generation using a Gaussian signal model and derives the decay rate of uncorrelated cross terms as the output is averaged over multiple snapshots. Chapter 5 analyzes the performance of estimating the spatial spectrum by comparing the multiplicative and min processing of the Elba data using the designed coprime and nested arrays. Chapter 6 contains a brief conclusion to the thesis and provides further directions for research.

Chapter 2: Background

This chapter describes the details of the shallow water passive sonar experiment used to compare the performance of coprime and nested array processors. The first section provides a short overview of the experiment, which was performed North of Elba Island near Italy. Gingras describes the details of the experiment in a short technical report [25]. Section 2.2 reviews the conventional processing of the Elba data using the Vertical Linear Array (VLA) to estimate the spatial spectrum. Sections 2.3 and 2.4 introduce the multiplicative and min processors using the coprime and nested array configuration. The remainder of this chapter compares the multiplicative and min beampatterns to the conventional ULA beampattern and identifies some of the issues with the traditional design formulation for nested and coprime arrays.

2.1 Elba Island data set

In 1993 SACLANT Center collected passive sonar data using a 48-sensor VLA deployed in the Mediterranean Sea north of Elba Island. The Signal Processing Information Base (SPIB) website [26] has recordings from 25 transmissions made over a 2-day period in October 1993. The local bathymetry shown in Figure 2.1 identifies the relative locations of the sensor array, stationary source, and the track of the ship deploying the towed source indicated by points A and B. In prior work researchers have used this data set to assess environmental inversion techniques [27] and robust matched field beamforming algorithms in shallow water environments [28, 29, 30].

The depth of the water column at the array site was 127 m. The VLA made use of 2 m intersensor spacing. The first sensor was at a depth of 18.7 m and the last sensor at a depth of 112.7 m. Although the technical report contains plots indicating the array tilt the

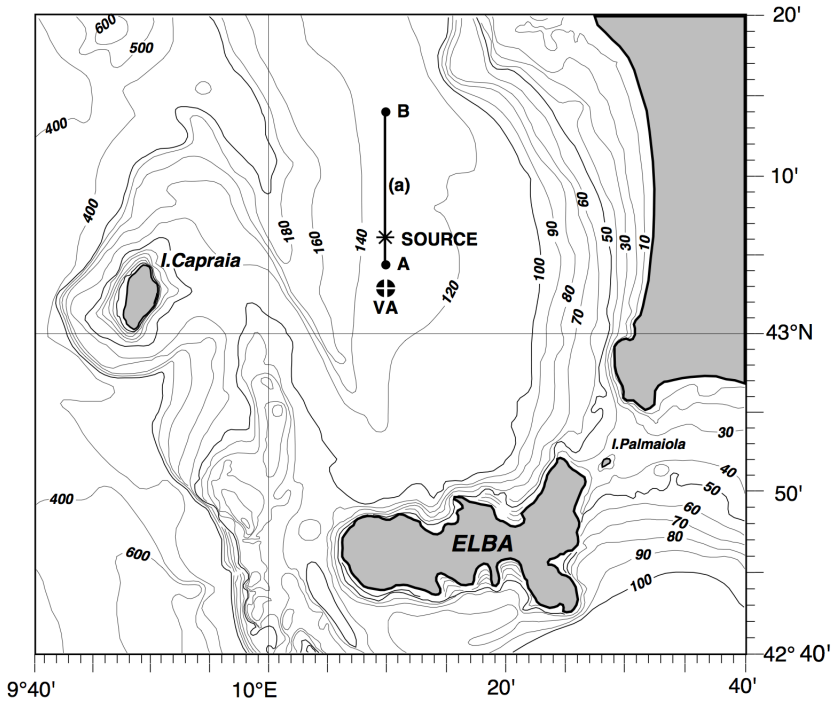

Figure 2.1: Bathymetry near Elba, location of the Vertical Array (VA) and the ship track.

exact sensor locations are not provided, thus tilt cannot be incorporated into the analysis described below.

A propagating signal with wavelength λ will be guaranteed to be free of spatial aliasing as long as the following condition holds

$$d \leq \lambda/2. \tag{2.1}$$

The wavelength λ is defined as $\lambda = c/f$ where c and f represent the speed of sound in water (reference $c = 1500$ m/s) and the temporal frequency of the propagating signal in Hertz, respectively. The maximum temporal frequency of a propagating signal sensed by the Elba VLA that is free of spatial aliasing is 375 Hz.

The stationary source (shown as "source" in the bathymetry plot in Figure 2.1) was located 5.8 km from the VLA at a depth of 79 m. Figure 2.2 shows the vertical underwater

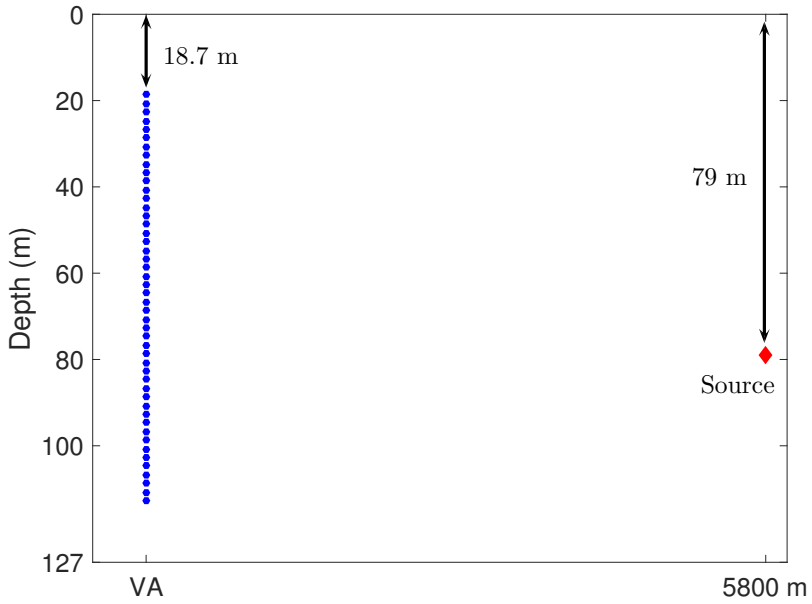

Figure 2.2: Vertical slit of the underwater column at the Elba array site indicating the individual sensor placement and the source location. The first sensor is at a depth of 18.7m from the surface.

column at the array site and the relative sensor and source positions as a function of depth and range in meters. The source transmitted maximal length sequences (pseudorandom sequences). The RM2 source transmissions processed in this thesis had a center frequency of 335 Hz and a bandwidth of ± 15 Hz around the center frequency.

2.2 Conventional Processing of the Elba data set

Each element of the ULA receives the pressure field transmitted by the stationary source. The characteristics of the stationary source are described in the previous section. The signal transmitted by the stationary source can be analyzed by computing the spectrogram of the signal received at any one sensor. The spectrogram of the data received at the first sensor i.e., at 18.7 m from the surface for the two signals with two different center frequencies is shown in Figure 2.3. The recording was 262 s long and used a sampling frequency,

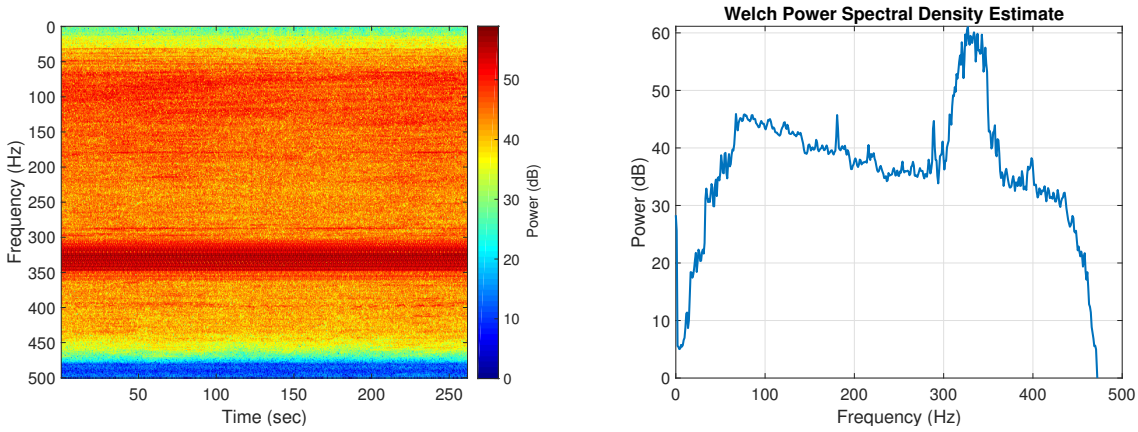

Figure 2.3: Spectrogram for a 262 s recording of psuedorandom signal at the first sensor with frequency and bandwidth 335 ± 15 Hz. The spectrogram was computed using a 1024-point Hanning window and 50% overlap.

$f_s = 1,000$ Hz. The spectrogram was obtained using a 1024-point Hanning window and a 50% overlap.

The spatial power spectrum can be obtained using a conventional ULA beamformer. The block diagram of the conventional beamformer is shown in Figure 2.4 where $\mathbf{x}, \mathbf{w}, \mathbf{y}$ represent the received narrowband signal vector, the spatial filter/beamformer and the beamformed output, respectively. A Welch-Bartlett approach splits the received data vector for each sensor into a number of blocks and the temporal spectra for each block is computed [31]. The input to the conventional processor is the narrowband data corresponding to the frequency bin of interest.

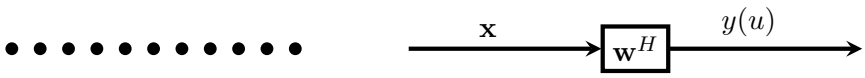

Figure 2.4: Block diagram of a conventional ULA beamformer where $\mathbf{x}$ represents the input vector for a single snapshot and the weights $\mathbf{w}^H$, the output of the beamformer steered to directional cosine u is given by $y(u)$.

VLAs can only resolve angles from 0 to 180 (because of the circular symmetry). The weight vector $\mathbf{w}$ can be expressed for each angle of arrival in the range, $0^o \leq \theta \leq 180^o$,

$$\begin{aligned} \mathrm{w}(n,\theta) &= w_t(n)\mathrm{v}(n,\theta), \\ &= w_t(n)\exp\left(-j\frac{2\pi}{\lambda}(n-1)d\cos(\theta)\right) \qquad \text{for} \quad n = 1,\ldots,L, \end{aligned} \tag{2.2}$$

where, $\mathbf{v}(\theta)$ represents the array manifold/replica vector for a plane wave with an angle of incidence θ using the given L sensor ULA with d m intersensor spacing, λ here represents the wavelength of the impinging wavefront. The array shading/tapering used is represented by $\mathbf{w}_t$.

Using the definition of directional cosine $u = \cos(\theta)$, the *visible region* for the directional cosine cis defined by $-1 \leq u \leq 1$. The weights for different directions in the visible region can be expressed in a matrix as shown below,

$$\mathbf{W} = \begin{bmatrix} \uparrow & & \uparrow \\ \mathbf{w}(-1) & \ldots & \mathbf{w}(1) \\ \downarrow & & \downarrow \end{bmatrix}_{L\times N_u} . \tag{2.3}$$

N_u is the number of discrete points in the visible region of the directional cosine vector (hence, the subscript u). The beamformer scans across the discrete points in u to provide a spatial response. The beampattern is the response from a single plane wave impinging the array at directional cosine, $u = u_s$. Mathematically, it can be expressed as

$$B_{u_l}(u_s) = \mathbf{w}^H(u_l)\mathbf{v}(u_s), \tag{2.4}$$

where $B_{u_l}(u_s)$ is the beampattern of the ULA steered to directional cosine u_l evaluated at u_s. Analogous to the frequency response of a time domain filter, the beampattern of a

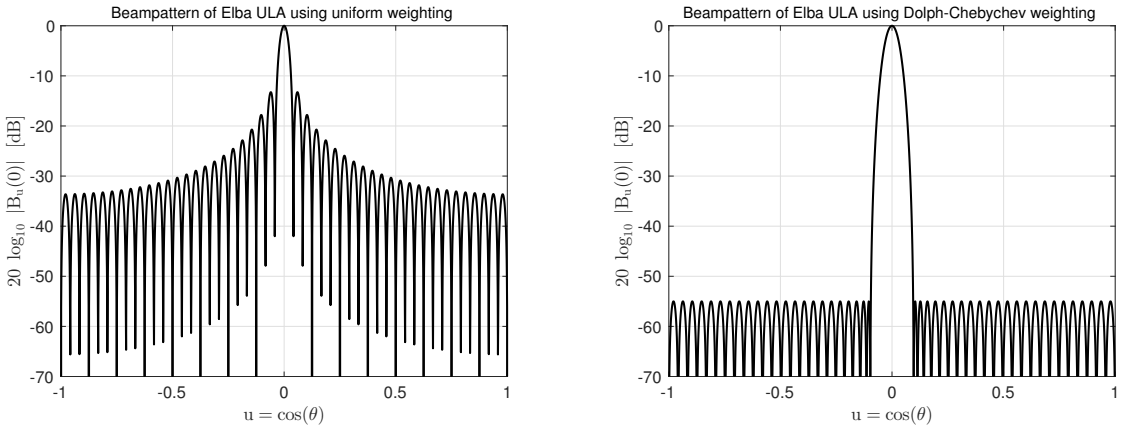

Figure 2.5: Conventional beampattern of the 48−sensor ULA using uniform weights normalized to obtain unity gain at source direction, $u = 0$.

ULA is the plane wave response of the designed spatial filter. The beampattern provides the user with essential information about the resolvability of two closely spaced sources in space and the ability to reject loud interferers or noise. By taking the squared magnitude of the beampattern, the received power can be expressed as a function of the directional cosine.

The weight vectors are normalized in two different ways so as to achieve either (a) unity gain in the source direction or (b) Power Spectral Density (PSD) [32]. Appendix B provides a detailed description of the two normalization schemes. The current discussion makes use of the weights normalized to obtain unity gain in the source direction. i.e., $\mathbf{w}/||\mathbf{w}||_1$[1]. Figure 2.5 illustrates the beampattern for the Elba ULA evaluated at $u_s = 0$ (broadside), assuming that $d = \lambda/2$. The left panel in the figure makes use of uniform tapering and the right panel make use of a Dolph-Chebychev tapering with sidelobe levels set to -55 dB.

Using the above designed beamformers one can compute the spatial power spectrum for the narrowband signals received by the Elba ULA. The narrowband signal for the RM2 source is generated using a Hanning window of block length= 500 samples and a 50%

[1] $||\mathbf{w}||_1$ denotes the $L1-$norm of the weight vector $\mathbf{w}$.

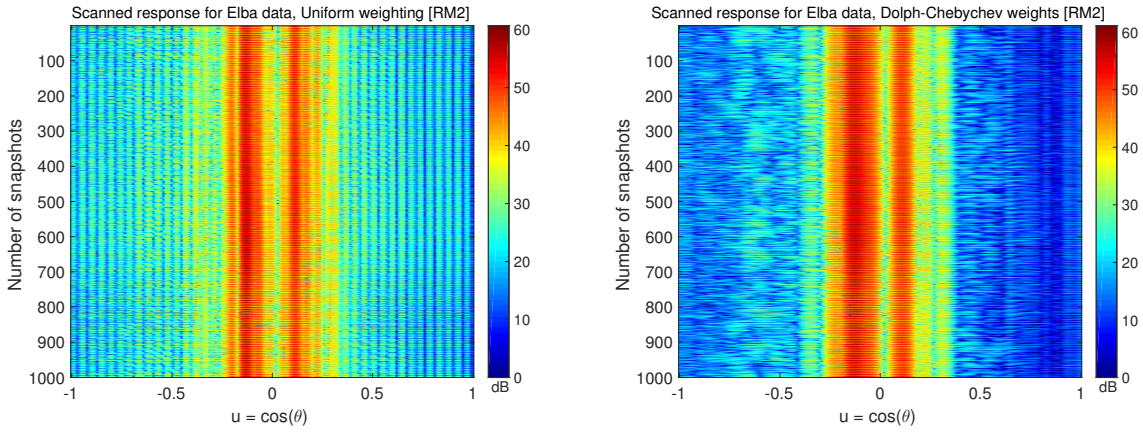

Figure 2.6: Scanned spatial response computed for the receptions of the Elba data RM2 source signal at the center frequency of 335 Hz using the beamformers designed with uniform and Dolph-Chebychev weights with sidelobe levels set to -55 dB.

overlap. A total of 1,000 snapshots were obtained for the narrowband signal with center frequency of 335 Hz. The *scanned response* is generated by steering the beamformer across different directions in the visible region for the narrowband signal at each time snapshot. The scanned spatial response computed using the beamformers designed with uniform and Dolph-Chebychev tapering is shown in Figure 2.6. The scanned response clearly indicates strong arrivals around broadside. Although uniformly tapered beamformers provide a beamwidth that is capable of separating closely spaced sources with ease, the peak sidelobe attained by these beamformers are only -13.5 dB down [33]. The Elba data presents a challenge due to the large dynamic range, which can be seen when the Dolph-Chebychev beamformer is applied. The response around endfire is significantly lower when compared to the response predicted using the beamformer with uniform tapering, indicating presence of weak sources outside of the strong arrivals around broadside. For the rest of this thesis, the conventional Dolph-Chebychev tapered beamformer will be used to analyze the Elba data using the ULA.

The *average scanned response* as the name suggests is the spatial spectrum averaged over a number of snapshots of the scanned response. Figure 2.7 illustrates the average over 1,000 snapshots of Elba data computed using the Dolph-Chebychev beamformer. The

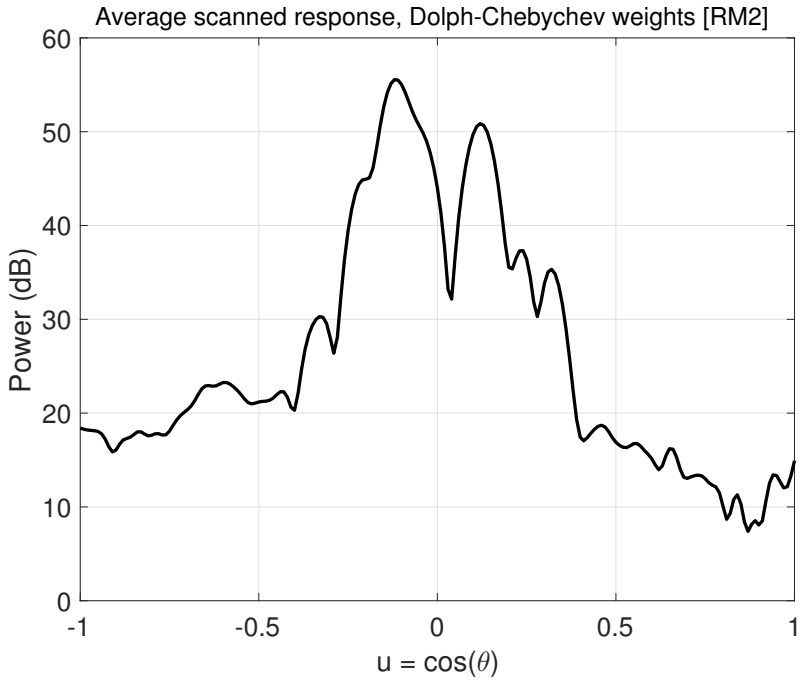

Figure 2.7: Average scanned response using the Dolph-Chebychev ULA beamformer for the RM2 signal at the center frequency of 335 Hz.

average scanned response is computed for the narrowband data at the center frequency of 335 Hz.

One of the most useful representations of the receptions made by a passive sonar VLA receiver is given by the wavenumber-frequency ($k - \Omega$) spectrum, which can be thought of as computing the averaged scanned spatial response at each frequency bin of the temporal spectra. A faster way to compute the wavenumber-ferquency spectra is to obtain a 2-D FFT of the receptions made by the ULA [34]. Figure 2.8 shows the wavenumber-frequency (k-Ω) spectra for the 262 s reception of the 335 Hz (RM2) signal from the stationary source. These plots were generated using conventional wavenumber-frequency processing of 1-second blocks of data and averaging the results over blocks. The processor used a 1024-point Hanning window in the time domain and a 48-point Dolph-Chebychev window with -55 dB sidelobes in the spatial domain. The plots reveal the general characteristics

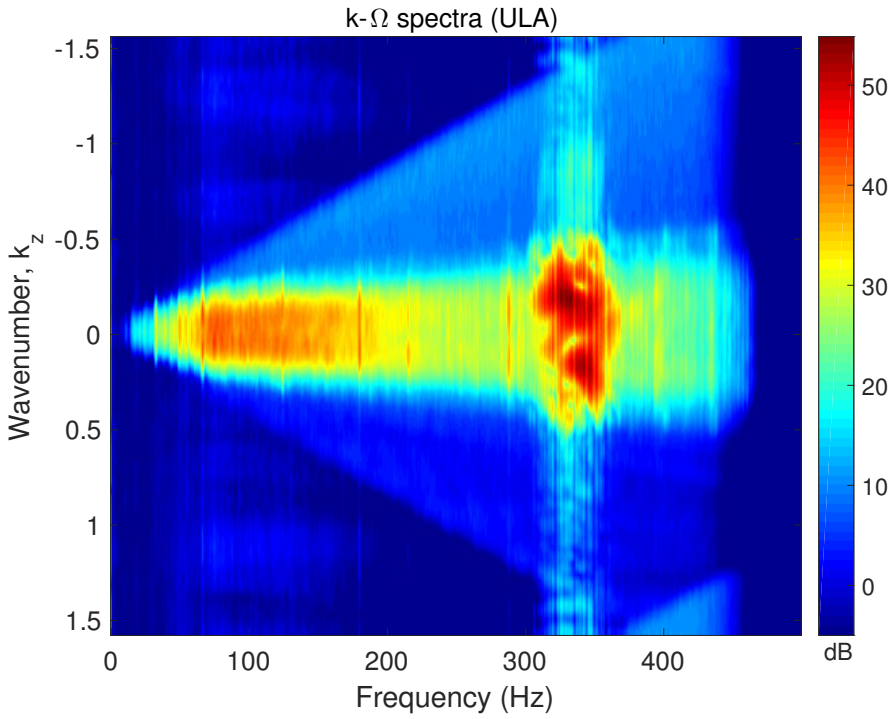

Figure 2.8: Wavenumber-frequency (k-Ω) spectrum for a 262 s recording of psuedorandom signal centered at 335 Hz, broadcast from the stationary source. The spectrum was computed using conventional processing of the data received by the 48-sensor ULA.

of the background noise. The noise is concentrated near $k_z = 0$, indicating that the noise field is dominated by low angle rays or trapped modes. These results agree with Krolik's observations about the data set [30].

2.3 Coprime Sensor Arrays

Vaidyanathan and Pal [21] proposed an approach using Coprime Sensor Arrays (CSAs) that reduces the number of sensors without compromising resolution. A coprime sensor array uses two interleaved undersampled uniform linear arrays with a relatively small number of sensors to obtain resolution comparable to a single densely populated ULA. The two subarrays consist of M and N sensors, with intersensor spacings of Nd and Md, respectively.

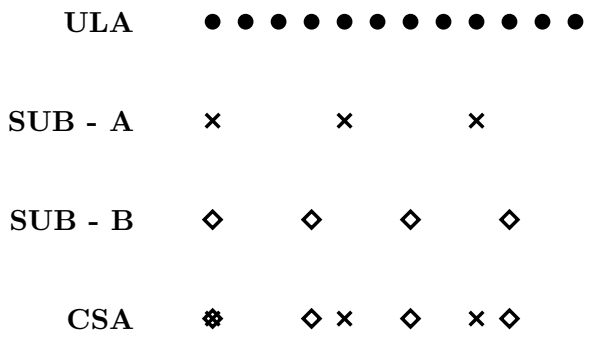

Figure 2.9: Array geometry for a 12 sensor ULA and 6 sensor CSA with coprime factors $M = 3$ and $N = 4$. The first element is common to both subarrays.

M and N are coprime integers, i.e., the greatest common divisor is 1. Figure 2.9 shows the sensor locations for the CSA subarrays designed to sample the same aperture as an L-sensor ULA. For this example, the ULA has 12 sensors, and the coprime factors are $M = 3$ and $N = 4$. The first sensor is shared by both subarrays.

In order to obtain the response using a CSA, one can make use of the *multiplicative processor* as shown in Figure 2.10. Where $\mathbf{x}$, $\mathbf{w}$ and $\mathbf{y}$ correspond to the received input signal vector, the spatial filter and the beamformed output, respectively. The subscripts A and B denote the two subarrays of the CSA. The CSA response is generated by multiplying the outputs of the individual subarrays processed independently using conventional beamformers (as described in the previous section). A multiplicative beampattern (response to a

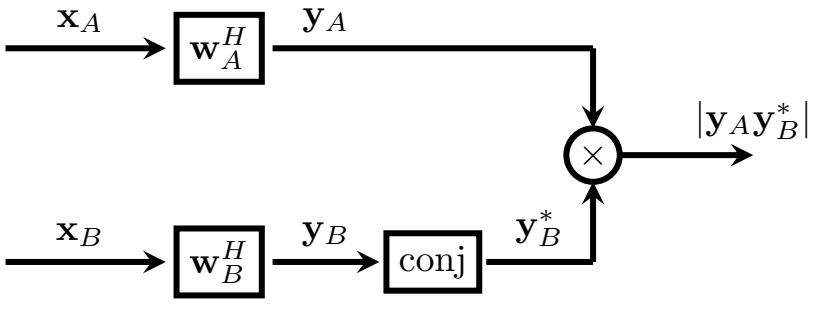

Figure 2.10: Block diagram of the multiplicative processor.

single plane wave) can be generated by multiplying the individual subarray beampatterns. The beampatterns of subarray-A processed using a conventional processor designed with uniform tapers is defined as

$$B_{A,u_l}(u_s) = \frac{\mathbf{v}_A^H(u_l)\mathbf{v}_A(u_s)}{M}, \tag{2.5}$$

where $B_{A,u_l}(u_s)$ is the beampattern of subarray-A steered to directional cosine u_l and evaluated at $u = u_s$ and $\mathbf{v}_{\mathrm{A}}(u_s)$ is the replica vector for subarray-A steered to directional cosine $u = u_s$, i.e., $\mathrm{v}_{A,u_s}(m) = \exp(j\frac{2\pi}{\lambda}u_s(m-1)Nd)$ for $m = 1, 2, \ldots, M$. Note that the weight vectors are normalized to guarantee unity gain in the source direction, i.e., when $u_l = u_s$, $B_{A,u_s}(u_s) = 1$. Similarly, we can express the beampattern of subarray-B as

$$B_{B,u_l}(u_s) = \frac{\mathbf{v}_B^H(u_l)\mathbf{v}_B(u_s)}{N}, \tag{2.6}$$

where $B_{B,u_l}(u_s)$ is the beampattern of subarray-B steered to directional cosine u_l and evaluated at $u = u_s$ and $\mathbf{v}_{\mathrm{B}}(u_s)$ is the replica vector for subarray-B steered to directional cosine $u = u_s$, i.e., $\mathrm{v}_{B,u_s}(n) = \exp(j\frac{2\pi}{\lambda}u_s(n-1)Md)$ for $n = 1, 2, \ldots, N$. The multiplicative beampattern is obtained by multiplying (2.5) and (2.6), i.e.,

$$B_{A,u_l}(u_s)B^*_{B,u_l}(u_s). \tag{2.7}$$

Figure 2.11 compares the beampatterns for the 12-sensor ULA and 6-sensor CSA shown in Figure 2.9. Assuming that the ULA sensor spacing d is less than half-wavelength ($\lambda/2$), the ULA results are guaranteed to be free of spatial aliasing. However, the CSA subarrays will be aliased since their spacings (Nd and Md) are more than half-wavelength. In order to compare the multiplicative beampattern with the conventional ULA beampattern, the squared magnitude of the conventional ULA beampattern is compared to the magnitude

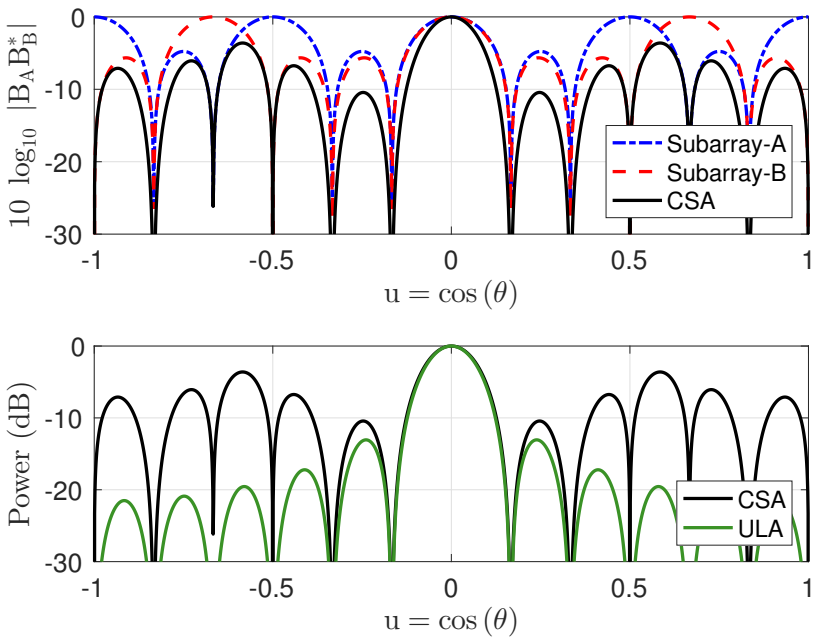

Figure 2.11: The top plot shows the beampattern of the CSA (solid black) formed by multiplication of the beampatterns of subarray-M (dashed blue) and subarray-N (dashed red). The bottom plot compares it to the beampattern of a 12-sensor ULA (dashed green).

of the multiplicative CSA beampattern. An equivalent multiplicative formulation of the ULA beampattern can be thought of as taking the magnitude of the product of the ULA beampattern with its conjugate.

The beampattern properties of a beamformer designed with uniform weights are well established. The null-to-null beamwidth of the ULA beamformer, $BW_{NN} = 2\lambda/Ld$. Similarly, the null-to-null beamwidth of the CSA subarray beamformers are $2\lambda/MNd$ and $2\lambda/NMd$ respectively for subarray-A and subarray-B. Since the multiplicative beampattern will also have similar beamwidth, this gives us the first and most important constraint to guarantee CSA designs that achieve similar resolution as an $L-$sensor ULA, i.e., $MN = L$ [35]

$$\frac{2\lambda}{MNd} = \frac{2\lambda}{Ld}. \tag{2.8}$$

Since the CSA subarrays are undersampled by factors M and N, the subarrays will have grating lobes (aliased copies) at intervals of λ/Nd and λ/Md for subarray-A and subarray-B, respectively. The grating lobes in the top panel of Figure 2.11 can be seen to be located at $u = \pm 0.5$ and $u = \pm 0.667$ when $u_s = 0$ and $d = \lambda/2$ for the CSA design $(M, N) = (3, 4)$. Due to the coprimality of M and N these grating lobes never intersect and the multiplication of the two beampatterns helps to successfully eliminate the ambiguity due to undersampling. The multiplicative CSA beampattern (shown in solid black) is the multiplication of the subarray beampatterns, and it does not contain grating lobes. The bottom panel in Figure 2.11 compares the conventional ULA beampattern with that of the multiplicative beampattern. The beamwidth of the CSA is equivalent to the ULA. Unfortunately, the sidelobes of the CSA beampattern are substantially higher than those in the ULA beampattern. This motivates a detailed study to design multiplicative beamformers using different tapers, preferably adjustable windows like the Dolph-Chebychev, to gain significant control over the beampattern properties [33].

2.4 Nested Arrays

Similar to the CSA, Nested Arrays (NAs) also incorporate the interleaved subarray design. In particular, the nested array designs used in this thesis make use of a 2-level nest, the *outer* nest/subarray makes use of P sensors with Qd spacing, whereas, the *inner* nest/subarray makes use of Q sensors with d spacing. The outer subarray is the aliased subarray, which, if processed independently, has grating lobes or copies of the source signal at the grating lobe locations in the spatial spectrum. The inner subarray which does not occupy the entire aperture of the ULA provides a large beamwidth (since the beamwidth is inversely proportional to the aperture spanned by the linear array/subarray). By using a multiplicative processor as shown in Figure 2.10, the ambiguity produced by the grating lobes can be reduced effectively. As an example, consider generating the multiplicative beampattern for a 6 sensor NA as shown in Figure 2.12. The inner subarray makes use of 3 sensors with d

Figure 2.12: Array geometry for a 12 sensor ULA and 6 sensor NA with the inner nest using $Q = 3$ sensors with d m spacing and the outer nest with $P = 4$ sensors and $3d$ m spacing. The first element is common to both subarrays.

m spacing (the same spacing as the ULA) and the outer subarray occupies an aperture of $(4-1) \times 3d$ using 4 sensors with $3d$ m spacing.

The multiplicative beampattern for the 6 sensor NA design is shown in Figure 2.13. The two important beampattern properties that provide us with a comparison to the 12 sensor ULA are the beamwidth and the peak sidelobe level attained by the NA design using multiplicative processing. The beamformers designed using uniform weights are normalized in order to obtain unity gain in the source direction for the NA subarrays and the ULA [32]. The beamwidth of the multiplicative processor is predicted by the beamwidth of the outer subarray (it occupies a larger aperture than the inner subarray), comparing the null-to-null beamwidth attained by the ULA and the outer subarray,

$$\frac{2\lambda}{PQd} = \frac{2\lambda}{Ld}. \tag{2.9}$$

The above equation provides the important constraint to obtain NA designs which attain similar resolution as an L sensor ULA, i.e., $PQ = L$. The inner subarray has a null-to-null beamwidth of $2\lambda/Qd$, i.e., when the beampatterns are evaluated at $u_s = 0$, the first null of the beamwidth occurs at $u = -\lambda/Qd$ and $u = +\lambda/Qd$, the nulls coincide exactly with the grating lobe locations of the outer subarray which are present at intervals of λ/Qd in u

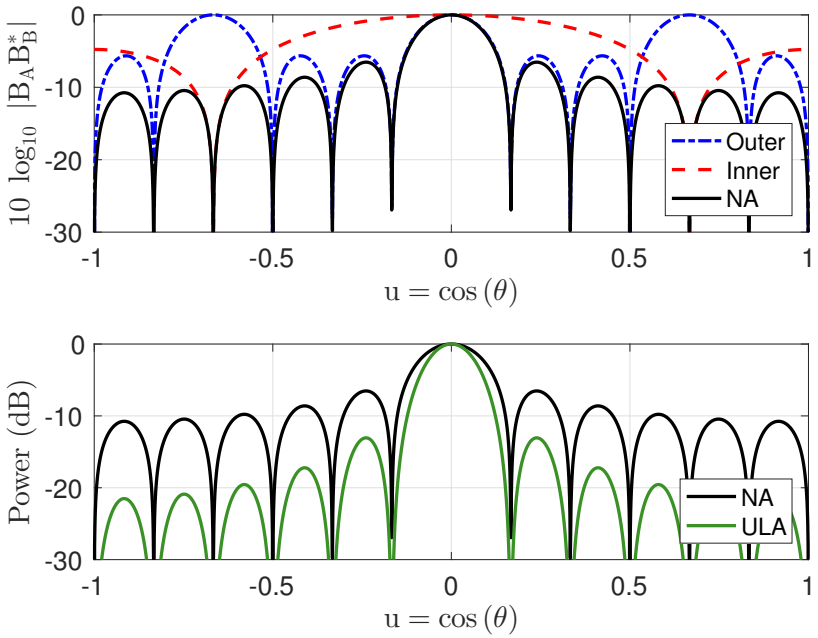

Figure 2.13: The top plot shows the beampattern of the CSA (solid black) formed by multiplication of the beampatterns of subarray-M (dashed blue) and subarray-N (dashed red). The bottom plot compares it to the beampattern of a 12-sensor ULA (dashed green).

space. The multiplicative beampattern which is obtained by multiplying the two subarray beampatterns, eliminates the ambiguity produced by the grating lobe due to the inherent null-grating lobe cancellation offered by the NA design.

The ULA beampattern $B_u(u)$ is expressed in terms of the power received from different angles/directions by taking the squared magnitude of the beampattern, $|B_u(u)|^2$. Using $10\log_{10}|B_u(u)|^2$, the beampattern can be express the power in units of decibels (dB). However, the multiplicative CSA beampattern is computed by multiplying the two individual subarray beampatterns, i.e., let $B_{A,u}(u)$ and $B_{B,u}(u)$ be the two individual subarray beampatterns for subarray-A and subarray-B, respectively. The CSA multiplicative beampattern can be given as, $B_{A,u}(u) \cdot B^*_{B,u}(u)$. The power pattern can be obtained using the CSA multiplicative beampattern by taking, $10\log_{10}|B_{A,u}(u) \cdot B^*_{B,u}(u)| = 10\log_{10}|B_{A,u}(u)| + 10\log_{10}|B_{B,u}(u)|$.

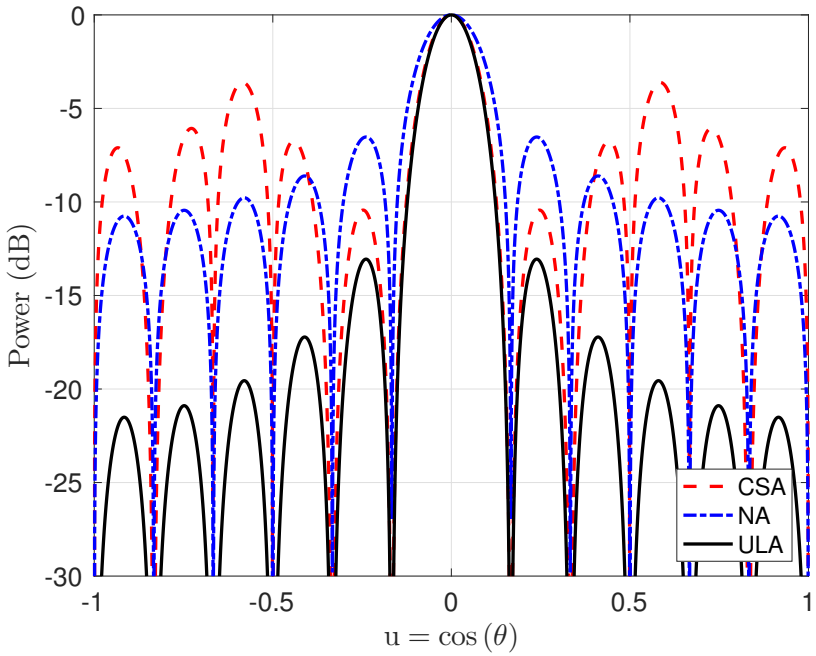

Figure 2.14: Comparison of the multiplicative beampatterns achieved using a 6 sensor CSA and NA as discussed in the previous sections to the conventional beampattern achieved using the 12 sensor ULA.

Figure 2.14 compares the multiplicative beampatterns generated using the 6 sensor NA and CSA to that of the 12 sensor ULA. Both the sparse arrays achieve similar beamwidth as the 12 sensor ULA processed using a conventional beamformer. Although the NA beamwidth is slightly wider than the CSA and ULA due to the presence of the non-aliased inner subarray, which occupies a short aperture providing with a wider beamwidth. The sidelobe levels in the multiplicative beampatterns are quite high when compared to the ULA beampatterns. The NA design provides a much more smoothed sidelobe structure due to the null-grating lobe cancellation as described, whereas the coprime design relies on the cancellation of the non-intersecting grating lobe locations (since grating lobe locations depend on the coprime factors) resulting in a non-uniform sidelobe structure.

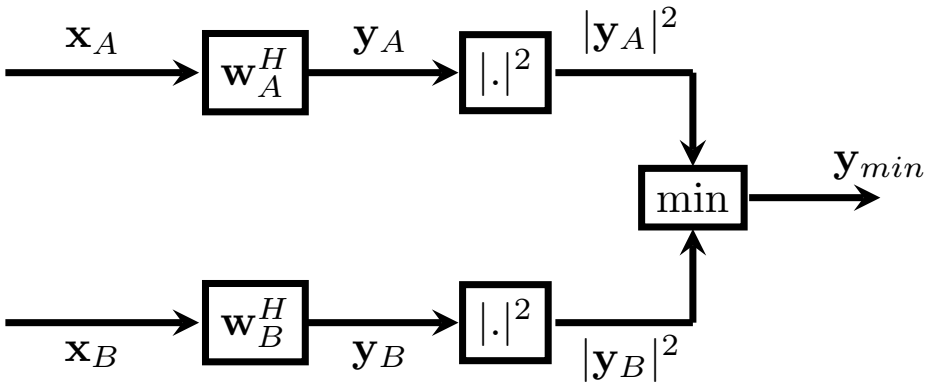

Figure 2.15: Block diagram of the min processor.

2.5 Min processor

In recent literature Liu and Buck introduced an intuitive approach to estimate the spatial spectrum from the individual subarrays of the CSA using a min processor [24]. Figure 2.15 shows a block diagram for the min processor, where $\mathbf{x}, \mathbf{w}, \mathbf{y}$ represent the received signal vector, the spatial filter/beamformer and the beamformed output, respectively. The output of the min processor is obtained by taking the minimum between the spectral estimates obtained by processing the two subarrays independently, i.e.,

$$\mathrm{y}_{min}(u) = \min(|\mathrm{y}_A(u)|^2, |\mathrm{y}_B(u)|^2). \tag{2.10}$$

The *min beampattern* is obtained by taking the minimum between the two subarray beampatterns (squared magnitude of the beampatterns). As an example, the min beampattern computed for the 6 sensor NA and CSA designs is compared in Figure 2.16. As noted by Liu and Buck, the min processor provides reduction in the sidelobe levels when compared to the multiplicative beampattern.

2.6 Summary

This chapter provided the background required to design the coprime and nested arrays for the Elba ULA. By analyzing the Elba data using the 48 sensor Elba ULA, the conventional beamformer acts as a benchmark for the design of the multiplicative and min processors. It is evident from the initial formulation of the CSA and NA designs, that although the beampattern of these sparse processors attain similar resolution, the peak sidelobe of the multiplicative and min CSA/NA beampatterns are significantly higher than the beampattern of the fully populated ULA obtained using a conventional processor.

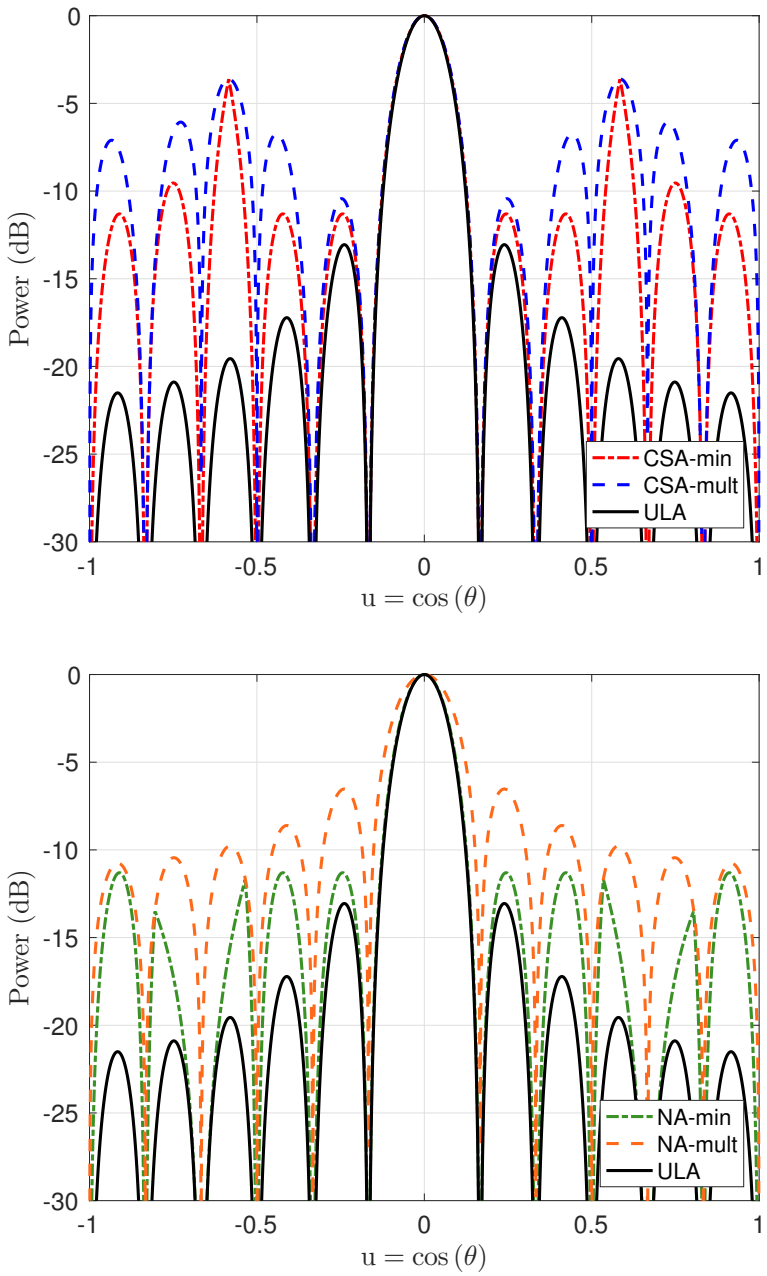

Figure 2.16: Comparison of the multiplicative vs. min vs. ULA beampattern for the 6 sensor CSA and NA designed as in Figure 2.9. Each beampattern is expressed in decibels, the power response of the min processors can be obtained by taking $10\log_{10}$ squared magnitude of the output, whereas, the power response from the multiplicative processors can be obtained by taking $10\log_{10}$ magnitude of the output. The multiplicative and min beampatterns are compared to the 12 sensor conventional ULA beampattern.

Chapter 3: Coprime and nested geometries for the Elba ULA

The previous chapter introduced the CSA and NA designs within a general array processing framework and illustrated the generation of multiplicative and min beampatterns. As mentioned in the text by Van Trees, the beampattern of an array is a crucial factor in evaluating its performance [1]. The purpose of this chapter is to explore the design of coprime and nested array geometries for the 48−sensor ULA used in the Elba experiment and select suitable CSA and NA designs by comparing the multiplicative and min beampatterns to the conventional ULA beampattern.

It is clear from the preceding discussion that although the multiplicative processors attain similar resolution as the conventional ULA processor, they fail to achieve similar peak sidelobe levels. This problem was investigated by Adhikari et al. who showed that by extending the subarrays and applying tapers it is possible to achieve a multiplicative beampattern with similar properties to a ULA beampattern [23]. Adhikari et al.'s approach allowed arbitrary extension of the subarrays. Since we wish to estimate the Elba spectrum using the designed CSA and NA, the extension of the subarrays must be restricted to the aperture of the Elba ULA.

Designing coprime and nested arrays to analyze the Elba data set requires a strategy to tackle the issue of high peak sidelobes posed by the multiplicative beamformers. When analyzed using the conventional ULA, the Elba data showed a large dynamic range (40 - 50 dB) of signal powers in the received data. This indicates that the desired beamformer peak sidelobe levels should be -55 dB or less (the ULA beamformer made use of -55 dB Dolph-Chebychev tapering).

This chapter explores all possible designs of the coprime and nested array geometries for the fixed aperture ULA used in the Elba experiment and compares the beampattern

performance of each design with the conventional ULA beampattern. The selection of the "best" coprime and nested array is shown to be a tradeoff between the total number of sensors and beampattern performance.

Section 3.1 provides a detailed explanation of the coprime array design for the Elba ULA. Note that this research appeared in a paper presented at the Asilomar Conference on Signals, Systems and Computers (SS&C) in 2014 [36]. Section 3.2 shows all possible designs for the nested configuration of the Elba ULA. Section 3.3 illustrates the min processor applied to each of the selected CSA and NA designs. Section 3.4 provides a comparison of each of the chosen CSA/NA designs by comparing the beampatterns obtained using multiplicative and min processors. The design criteria is focused on satisfying two major beampattern properties, (a) peak sidelobe level achieved should be at least -55 dB and (b) each designed beamformer should attain similar beamwidth for further comparison of the estimated spatial spectrum in the later chapters.

3.1 Coprime array design for the Elba ULA

In previous work [23], the number of sensors added to each subarray was selected to reduce sidelobes by extending the array *outside* of that fixed aperture. The Elba Island ULA has 48 elements, spanning an aperture of $47d$, where $d = 0.44\lambda \approx \lambda/2$ for the 335 Hz source. In this study the goal is to design the CSA such that the the extended subarrays fit within the total aperture, i.e., $(M_e - 1)Nd \leq 47d$ and $(N_e - 1)Md \leq 47d$, where, M_e and N_e are the total number of sensors in each extended subarray. As we add more sensors to the subarrays the aperture increases, this increase in aperture in turn provides a reduction in the width of the main lobe and the grating lobe, the peak sidelobe of the multiplicative beampattern is caused due to the interaction of the grating lobes. Hence, it is essential to extended the subarrays as much as possible in order to accommodate for the high dynamic range in the Elba data.

To design a CSA that has the resolution of an $48-$sensor ULA, the coprime integers M

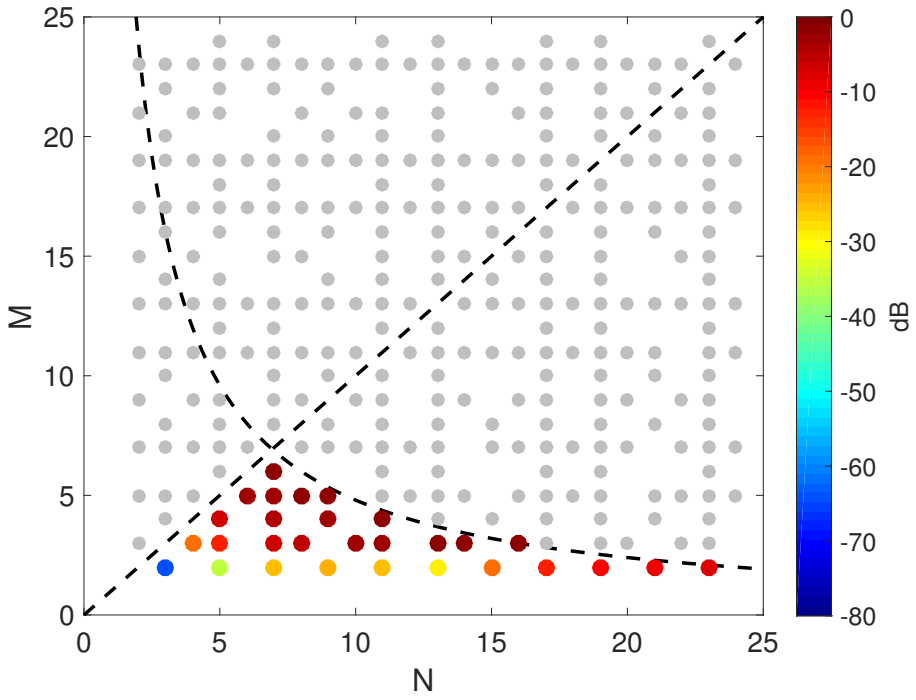

Figure 3.1: Coprime integer pairs for $1 \leq M \leq 25$ and $1 \leq N \leq 25$. The dashed-blue lines indicate the constraints $MN = 48$ and $M = N$. Each point is associated with extension factors that would fit the $47d$ aperture of the full ULA. The colorbar represents the peak sidelobe level in dB for each design.

and N are chosen such that

$$MN \leq 48. \tag{3.1}$$

Adhikari et al. [23] showed that to minimize the total number of sensors, M and N should be as close to equal as possible, i.e., $N = M + 1$. The scatter plot shown in Figure 3.1 provides all possible co-prime pairs for $1 < M < 25$ and $1 < N < 25$ that satisfy the given constraints for the Elba ULA. Without loss of generality, assume that $N > M$, thus the coprime pairs of interest lie to the right of the dashed line. There are 29 coprime pairs that satisfy the basic constraint given by equation (3.1). Each coprime pair is associated with extension factors determined by extending both the subarrays to fit inside the $47d$ aperture. The points closest to the intersection of the two constraints provide the desired resolution with the smallest number of sensors. Extension factors for the subarrays increase as we

move away from the constraint lines (dashed-black). The color of the circles represents the peak sidelobe level (dB) achieved by each CSA design determined by a coprime pair. The sidelobe levels were computed by searching for the minimum sidelobe level achievable using Dolph-Chebychev shading on the two subarrays.

The coprime design using $M = 6$, $N = 7$ is the closest to the intersection of the two constraint lines. This design uses extension of each subarray by one sensor to fit inside the $47d$ aperture. Figure 3.2 shows the sensor placement and the effective beampatterns for the subarrays and the CSA. This coprime design uses the smallest number of sensors to span the aperture, i.e., 14 sensors ($\approx 70\%$ reduction in the number of sensors compared to the full ULA). The lowest peak sidelobe of -6 dB was achieved when the subarrays were tapered with a Dolph-Chebychev window set to -12 dB sidelobes.

The CSA design using coprime factors $M = 2$ and $N = 3$ allows for the largest extension of the two subarrays and results in the lowest peak sidelobe for the given constraint on ULA aperture. Figure 3.3 shows the sensor placement and the beampatterns for this configuration. In this design subarray-A has 16 sensors with $3d$ spacing and subarray-B has 24 sensors with $2d$ spacing. The CSA contains 32 sensors, which is a 33% reduction compared to the 48-sensor ULA. Of the 29 possibilities shown in Figure 3.1, this design achieves the lowest peak sidelobe level of -65 dB when the two subarrays are tapered with a Dolph-Chebychev windows of -130 dB sidelobes. The CSA design that shall be considered for analyzing the Elba data will make use of subarrays tapered with -110 dB sidelobes of the Dolph-Chebychev window. The resolution also improves by relaxing the peak sidelobe level requirement to the desired at -55 dB.

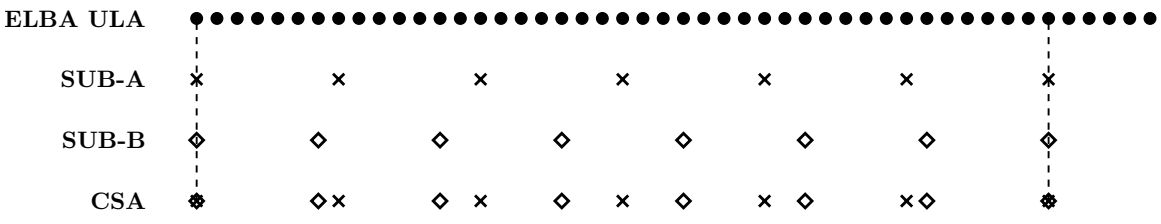

(a) Sensor placement

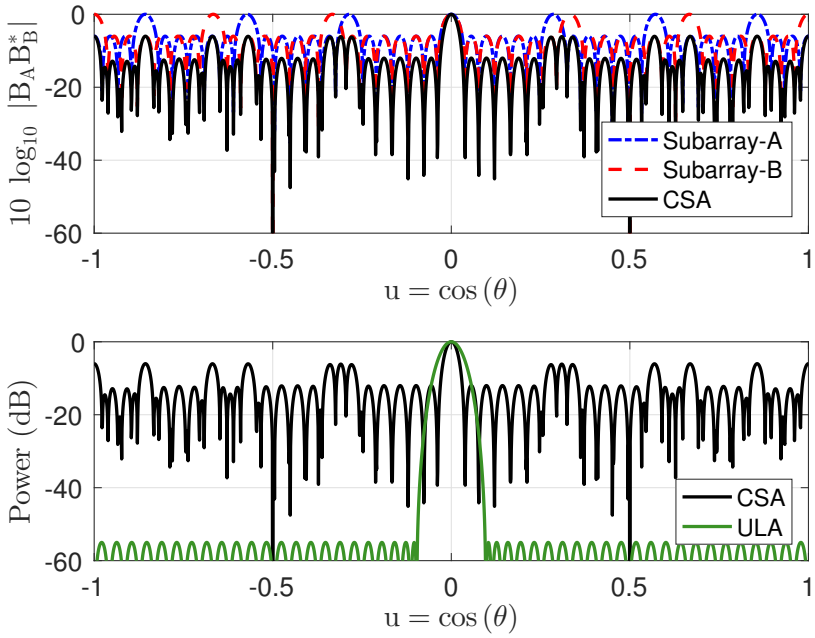

(b) Multiplicative beampattern

Figure 3.2: beampatterns for the CSA with $M = 6$ and $N = 7$ with a maximum extension by 1 sensor. The sensor placement is shown in (a) where the dashed lines indicate the shared sensors and (b) shows the multiplicative beampattern designed using subarray weights shaded with a Dolph-Chebychev window of -12 dB sidelobes (beampatterns for the coprime subarrays are also plotted on a $10\log_{10}$ scale).

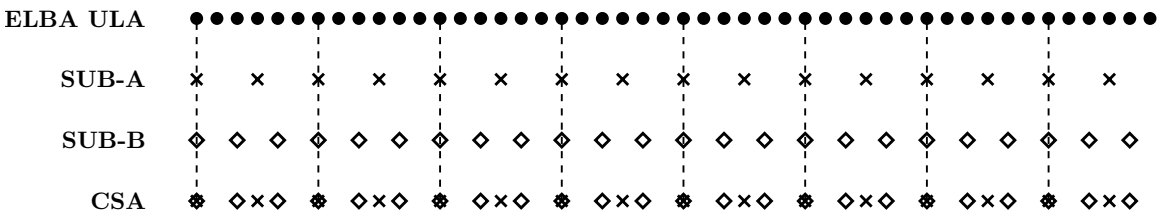

(a) Sensor placement

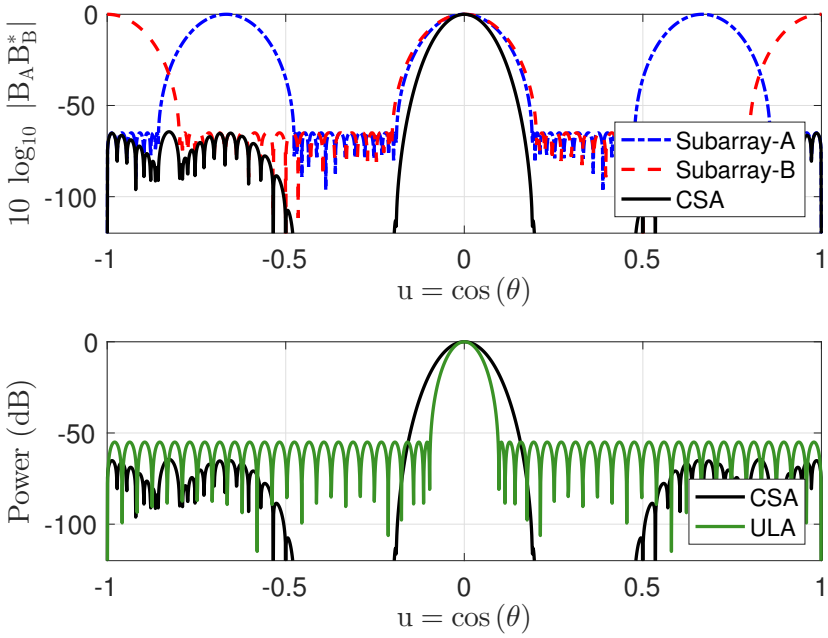

(b) Multiplicative beampattern

Figure 3.3: beampatterns for the CSA with $M = 2$ and $N = 3$ extended to fit inside the $47d$ aperture. The sensor placement is shown in a) where the dashed lines indicate the shared sensors and (b) shows the multiplicative beampattern designed using subarray weights shaded with Dolph-Chebychev windows of -130 dB sidelobes (beampatterns for the coprime array are plotted on a $10\log_{10}$ scale).

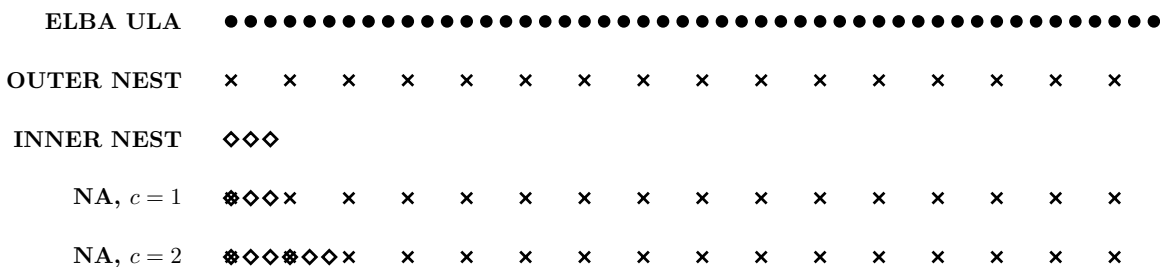

Figure 3.4: Sensor positioning of the NA designed for the 48-sensor ULA using $Q = 3$ and two extension factors $c = 1$ and $c = 2$.

3.2 Nested array design for the Elba ULA

The NA makes use of an undersampled outer subarray and a non-aliased inner subarray. The outer subarray makes use of P sensors with Qd spacing and the inner subarray uses Q sensors with d spacing. The aperture of the outer subarray dictates the resolution attained by the multiplicative beampattern. In order to ensure similar resolution as the 48-sensor Elba ULA, it is required that $PQ = 48$, i.e., for a given choice of Q the outer subarray is extended to span the aperture of $47d$. The number of sensors in the outer subarray can be obtained by

$$P = \left\lceil \frac{48}{Q} \right\rceil. \tag{3.2}$$

The peak sidelobe in the beampattern of an NA is the result of the interaction between the mainlobe of the inner subarray and the grating lobe of the outer subarray. By introducing more periods of the inner subarray, the width of the main lobe reduces and the interaction with the grating lobes results in lower sidelobes for the NA beampattern. The total number of sensors in the inner subarray can be given by cQ, where c is the extension factor. Figure 3.4 illustrates the sensor placement for a nested design using $Q = 3$ and two extension factors $c = 1$ and $c = 2$.

Figure 3.5 shows all possible nested array designs for the Elba ULA, the colorbar indicates the lowest possible sidelobe achieved (in dB) by the multiplicative beampattern for

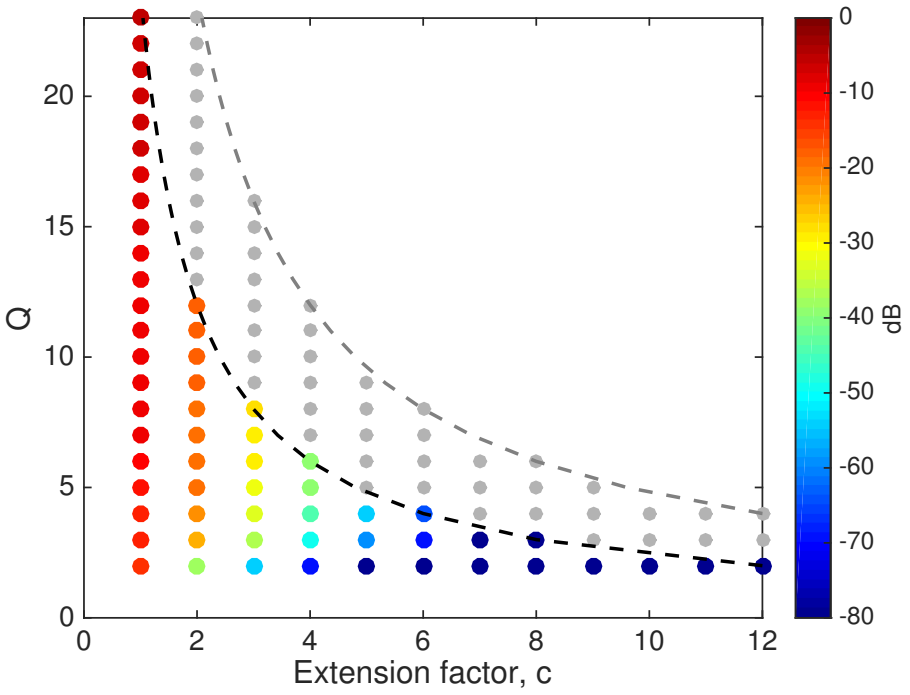

Figure 3.5: Nested array designs for the Elba ULA, $2 \leq Q \leq 24$ and $1 \leq c \leq 12$. The dashed-black lines indicate the constraint $cQ \leq 24$. The colorbar represents the peak sidelobe level in dB attained by each design.

each of the designs using Dolph-Chebychev shading of the two subarrays. The motivation in using Dolph-Chebychev weighting was the ability of this window to control the two beampattern parameters. The *black* dashed line represents a constraint, $cQ \leq 24$, to ensure that the inner subarray does not occupy more than half the aperture of the ULA. This is done as the goal of this research is to obtain a NA design that provides a reduction in the number of sensors compared to the ULA. The total number of sensors used in the nested array can be obtained by,

$$T_{na} = \left\lceil \frac{48}{Q} \right\rceil + cQ - c. \tag{3.3}$$

The nested design with parameters $Q = 3$ and $c = 8$ makes use of an inner subarray with

24 sensors and d spacing and the outer subarray uses 16 sensors with $3d$ spacing, a total of 32 sensors, i.e., a 33% reduction in the number of sensors compared to the ULA. The inner subarray of the designed NA spans half the aperture of the Elba ULA. In order to use this NA design to analyze the Elba data set, the inner subarray can span either the bottom/top portion of the Elba ULA or placing the inner subarray centered around the middle of the ULA. The ULA analysis of the Elba data indicates strong arrivals around broadside, which suggests placing the inner subarray centered around the middle of the ULA to guarantee symmetric sampling of the propagating modes. Placing the inner subarray at the bottom or top of the Elba ULA will ensure sampling of the modeshapes corresponding to higher or lower mode numbers, respectively [37].

Figure 3.6 shows the sensor placement and multiplicative beampattern for this NA design as well as the individual subarray beampatterns compared to the conventional ULA beampattern. This design achieves the desired peak sidelobe of -55 dB using Dolph-Chebychev tapering of the subarray weights.

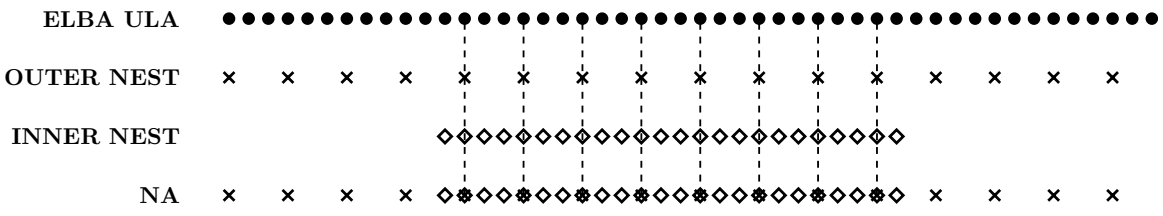

(a)

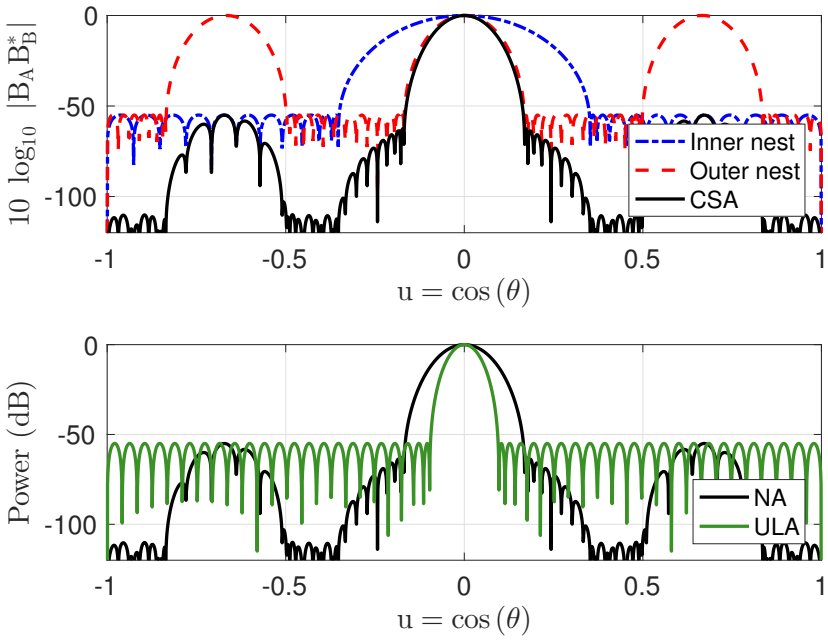

(b)

Figure 3.6: The sensor placement for the Nested array with $Q = 3$ and $c = 8$ is shown in (a) and (b) illustrates the multiplicative beampattern designed for subarrays tapered with Dolph-Chebychev shading of -110 dB sidelobes. Each of the subarray beampatterns are plotted on a $10\log_{10}$ scale.

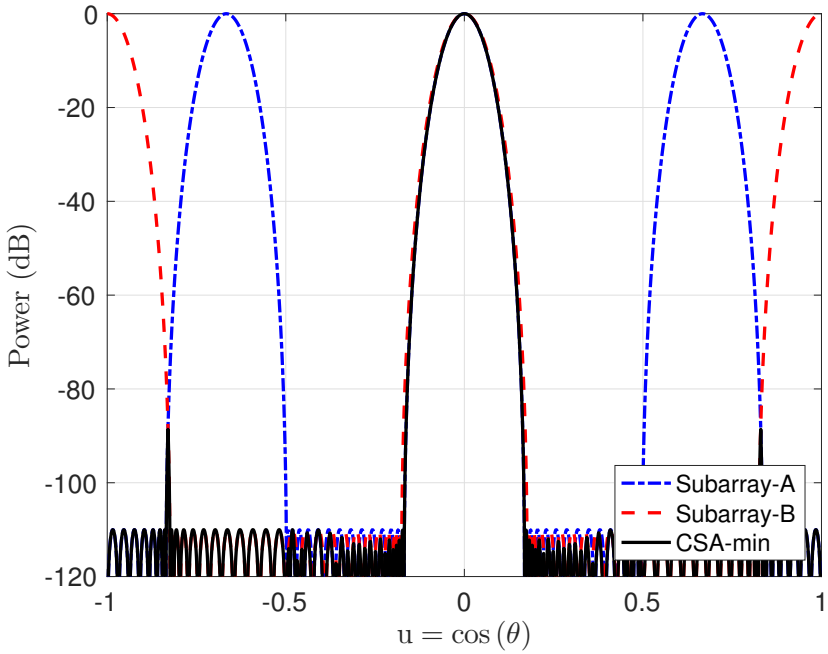

Figure 3.7: The designed CSA-min beampattern for subarrays tapered with Dolph-Chebychev window with -110 dB sidelobes. The peak sidelobe achieved by this processor is -88 dB.

3.3 Min beampatterns for the designed CSA/NA

The min processor generates the beampattern by taking the minimum of the squared magnitude of the two subarray beampatterns. The subarrays for this processor make use of Dolph-Chebychev tapers for the two designs with sidelobes set to -110 dB. The peak sidelobe level achieved varies for the two designs. The peak sidelobe in the CSA-min beampattern may be higher than -110 dB if there exists any overlap between the grating lobes of the two subarrays as shown in Figure 3.7. The peak sidelobe achieved by the CSA using a min processor is -88 dB.

The peak sidelobe of the NA-min beampattern may be greater than the subarray peak sidelobe of -110 dB if there exists an overlap between the grating lobe of the inner subarray and the main lobe of the outer subarray. The NA design as obtained in the previous section does not have any overlap between the grating lobe and main lobe providing a peak sidelobe

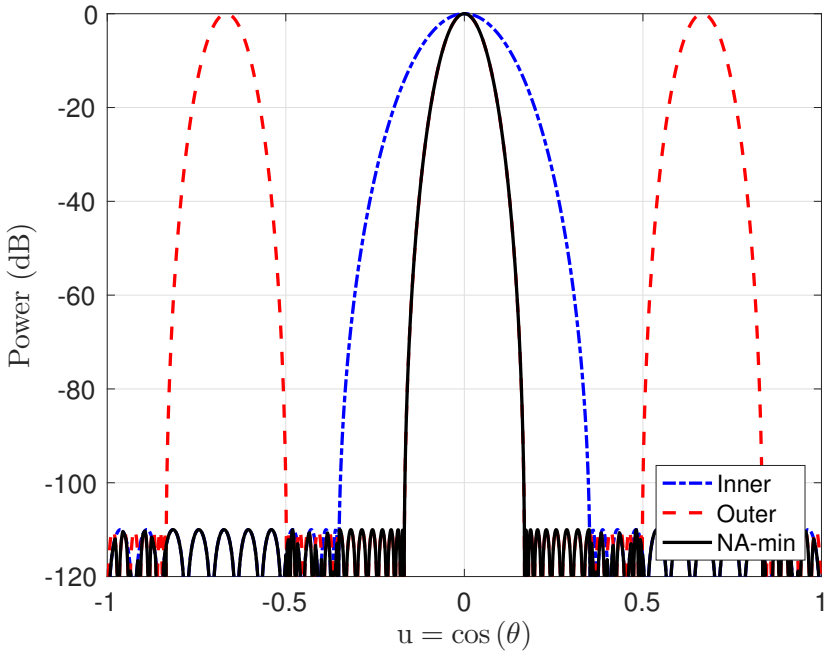

Figure 3.8: The designed CSA-min beampattern for subarrays tapered with Dolph-Chebychev window with -110 dB sidelobes. The peak sidelobe achieved by this processor is -88 dB.

of -110 dB as shown in Figure 3.8

3.4 Comparison of the multiplicative and min CSA/NA processors designed for the Elba ULA

The multiplicative beamformers designed in the previous sections achieve the desired peak sidelobe level of -55 dB when the subarrays are tapered with Dolph-Chebychev windows of -110 dB sidelobes. It is well known that the beamwidth and peak sidelobe level are inversely proportional to each other. The beamwidth of the designed multiplicative beamformers are wider when compared to the conventional ULA processor using Dolph-Chebychev tapers with sidelobes set to -55 dB.

The designed multiplicative beamformers provide sufficiently low peak sidelobe levels in order to discriminate between the strong and weak arrivals in the Elba data. In order

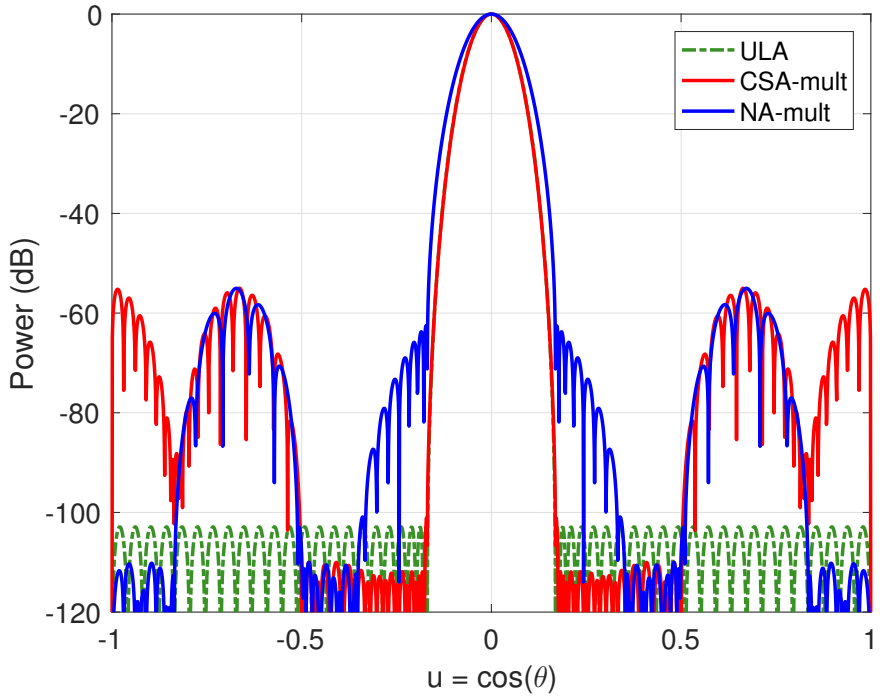

Figure 3.9: Comparison of the designed multiplicative CSA/NA beampatterns to the conventional ULA beampattern obtained using Dolph-Chebychev tapering. The conventional processor is fine tuned to achieve similar beamwidth as the multiplicative processors.

to provide even grounds of comparison with the conventional processors, it is essential to ensure the resolution/beamwidth attained by both processors is the same. Using adjustable tapers like the Dolph-Chebychev window grants the added advantage to tune the beamwidth by altering the sidelobe levels. Hence, the conventional ULA processor that shall be used for comparing the performance will make use of Dolph-Chebychev tapers with -103 dB sidelobes which ensures that the beamwidth attained by the multiplicative processors is the same as the conventional processor. Figure 3.9 compares the multiplicative CSA/NA beampatterns to the conventional processor providing with the equivalent beamwidth and desired peak sidelobe level. Although, the null-to-null beamwidth equivalence is ensured, the inner subarray of the designed NA provides with the expansion of the mainlobe structure in the resultant NA beampattern. The peak sidelobe achieved by each design is sufficiently low to compensate for the high dynamic range in the Elba data. Figure 3.10 compares the

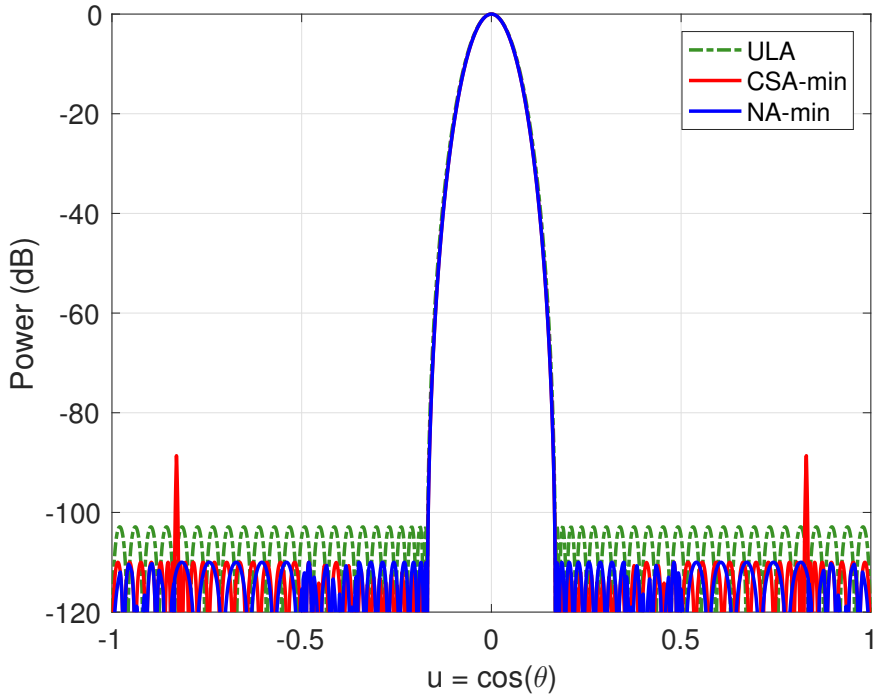

Figure 3.10: Comparison of the designed min CSA/NA beampatterns to the conventional ULA beampattern obtained using Dolph-Chebychev tapering.

min beampatterns of the designed CSA and NA to the conventional ULA beampatterns.

3.5 Summary

In summary, a ULA spans a fixed aperture of $(L-1)d$ using L sensors and d m spacing. A CSA design can be formulated by choosing appropriate values of the undersampling factors M and N, where M and N are coprime integers chosen to satisfy $MN \leq L$. The subarrays of the CSA span apertures of $(M_e - 1)Nd$ and $(N_e - 1)Md$, respectively. Subarray-A uses $M_e = \lceil \frac{L}{N} \rceil$ sensors with Nd spacing. Subarray-B uses $N_e = \lceil \frac{L}{M} \rceil$ with Md spacing.

The NA design requires a choice of the undersampling factor of the outer subarray, Q, such that the outer subarray spans the aperture of the ULA using $P = \lceil \frac{L}{Q} \rceil$ sensors with Qd spacing. The inner subarray is non-aliased and makes use of cQ sensors with d spacing,

where c is the extension factor. The constraint applied in the NA design restricts extending the inner subarray beyond half the aperture of the ULA, i.e., $cQ \leq L/2$, since extending the inner subarray beyond half the length of the ULA would be essentially the same as using the ULA itself.

This chapter presented the design of multiplicative and min CSA/NA processors to be used to analyze the Elba data set. The designed CSA/NA provide a 33% reduction in the number of sensors. The multiplicative and min beamformers successfully satisfy the two design criteria: (1) desired peak sidelobe ≤ -55 dB and (2) similar resolution, across all processors. Table 3.1 provides a comparison of the designed CSA/NA multiplicative and min beamformer properties with the conventional beamformer. The selected designs will be analyzed in the next chapter using a Gaussian signal model to highlight the issue with cross terms at the output of the multiplicative processors.

Table 3.1: Comparison of the multiplicative and min processors using the CSA and NA designed for the Elba ULA.

Processor Type	**Array design**	**Total no. of sensors**	**Peak sidelobe level in (dB)**	**Beamwidth BW_{NN} in u-space at $d = \lambda/2$**
Conventional processor	ULA	48	-103 dB	0.338
Multiplicative Processor	CSA	32	-55 dB	0.338
	NA	32	-55 dB	0.338
Min Processor	CSA	32	- 88 dB	0.338
	NA	32	-110 dB	0.338

Chapter 4: Narrowband simulation of designed CSA/NA multiplicative and min beamformers

The previous chapter was focused on selecting appropriate CSA and NA designs for the fixed 48−sensor Elba ULA. The selected designs are shown to provide the best tradeoff between the total number of sensors used and beampattern performance. The min and multiplicative beamformers were designed intelligently with prior knowledge of the Elba data analyzed using the ULA.

As noted in Chapter 1, multiplicative processors have been used widely in applications related to radio astronomy and radar since the 1960's. Ksienski and Pedinoff observed the presence of cross terms or cross products at the output of a multiplicative processor in multiple target/source scenarios for radar applications [18, 19]. Davies suggested averaging over multiple snapshots when the two targets/sources are uncorrelated to reduce their effect [20].

In this chapter we approach the issue of cross terms by identifying the different types of cross terms using a Gaussian signal model for a single source in spatially white noise. Adhikari and Buck studied the detection problem of a similar signal model using coprime arrays. Their work however was focused on the detection of the source signal of interest and they did not consider cross terms effects [38].

The output of the multiplicative processor is analyzed and the contribution of each term at the output is compared to the overall spatial spectrum estimate for a range of Signal-to-Noise Ratio (SNR) values. The analytical derivation for the decay of the uncorrelated cross terms is provided. The numerical simulations and analytical results are shown to have good agreement. The output of a min processor is computed by taking the minimum of the two subarrays processed independently. Since the output of at least one of the subarrays is

guaranteed to be aliased, this chapter will illustrate the cases when the min processor will fail to eliminate the ambiguity.

Section 4.1 illustrates the generation of cross terms at the output of a multiplicative processor using a narrowband signal model and identifies the locations of the cross term peaks in the visible spectrum. Section 4.2 provides the derivation of the cross term decay as the output of the multiplicative processor is averaged over snapshots. Section 4.3 shows the issues with estimating a spatial spectrum using the min processors.

4.1 Problem Formulation

Consider processing a plane wave source and noise using the 48−sensor Elba ULA. The direction of arrival of the signal wavefront at the array axis can be represented by the directional cosine $u_1 = \cos(\theta_1)$ where θ_1 is the angle of incidence. The signal amplitude s_1 is modeled as a zero-mean complex Gaussian random variable, $s_1 \sim \mathcal{CN}(0; \sigma_1^2)$ and $\mathbf{n}$ is the received noise vector modeled as a zero-mean complex Gaussian random vector, $\mathbf{n} \sim \mathcal{CN}(0; \sigma_n^2 \mathbf{I}_{L\times L})$. The signal and noise components are assumed to be independent of each other. The Signal-to-Noise Ratio (SNR) is defined as $\text{SNR} = \sigma_1^2/\sigma_n^2$. The input to the ULA is,

$$\mathbf{x} = s_1 \mathbf{v}_1 + \mathbf{n} \tag{4.1}$$

where $\mathbf{v}_1$ is the replica vector/array manifold vector corresponding to the ULA for the source arriving from the direction u_1, propagating with wavelength λ, i.e., $\text{v}_1(l) = \exp(j\frac{2\pi}{\lambda}u_1(l-1)d)$ for $l = 1, 2, \ldots, L$ [1]. The input to the individual subarrays of the CSA as designed in Figure 3.3 are defined as

$$\mathbf{x}_\text{A} = s_1 \mathbf{v}_{\text{A},1} + \mathbf{n}_\text{A}, \qquad \mathbf{x}_\text{B} = s_1 \mathbf{v}_{\text{B},1} + \mathbf{n}_\text{B}, \tag{4.2}$$

where $\mathbf{v}_{\text{A},1}$ and $\mathbf{v}_{\text{B},1}$ are the source replica vectors corresponding to subarray-A and subarray-B, respectively, i.e., $\text{v}_{A,1}(m) = \exp(j\frac{2\pi}{\lambda}u_1(m-1)Nd)$ for $m = 1, 2, \ldots, M_e$ and $\text{v}_{B,1}(n) =$

$\exp(j\frac{2\pi}{\lambda}u_1(n-1)Md)$ for $n = 1, 2, \ldots, N_e$. The received noise vectors $\mathbf{n}_\mathrm{A}$ and $\mathbf{n}_\mathrm{B}$, for subarray-A and subarray-B, respectively, are extracted from the ULA noise vector $\mathbf{n}$. The output from subarray-A can be evaluated as a function of the directional cosine u in the visible region, i.e., $-1 \leq u \leq 1$, by applying a spatial filter, $\mathbf{w}_\mathrm{A}$,

$$y_\mathrm{A}(u) = {\mathbf{w}_\mathrm{A}}^H \mathbf{x}_\mathrm{A} = s_1 \underbrace{{\mathbf{w}_\mathrm{A}}^H \mathbf{v}_{\mathrm{A},1}}_{B_{A,u}(u_1)} + {\mathbf{w}_\mathrm{A}}^H \mathbf{n}_\mathrm{A}. \tag{4.3}$$

$B_{A,u}(u_1)$ is the beampattern of subarray-A steered to directional cosine u evaluated at u_1. Similarly, the output of subarray-B can be evaluated by applying a corresponding spatial filter ${\mathbf{w}_\mathrm{B}}^H$,

$$y_\mathrm{B}(u) = {\mathbf{w}_\mathrm{B}}^H \mathbf{x}_\mathrm{B} = s_1 \underbrace{{\mathbf{w}_\mathrm{B}}^H \mathbf{v}_{\mathrm{B},1}}_{B_{B,u}(u_1)} + {\mathbf{w}_\mathrm{B}}^H \mathbf{n}_\mathrm{B}, \tag{4.4}$$

where $B_{B,u}(u_1)$ is the beampattern of subarray-B steered to u evaluated at u_1. The weights $\mathbf{w}_\mathrm{A}$ and $\mathbf{w}_\mathrm{B}$ are normalized such that the source signal is passed through the beamformer with unity gain [32]. The output of the multiplicative processor consists of four terms

$$\begin{aligned} y(u) = y_A y_B^* \quad &= |s_1|^2 B_{A,u}(u_1) B_{B,u}^*(u_1) + {\mathbf{w}_\mathrm{A}}^H \mathbf{n}_\mathrm{A} {\mathbf{n}_\mathrm{B}}^H \mathbf{w}_\mathrm{B} \\ &+ \underbrace{s_1 B_{A,u}(u_1) {\mathbf{n}_\mathrm{B}}^H \mathbf{w}_\mathrm{B}}_{cross\ term\ 1} + \underbrace{s_1^* B_{B,u}^*(u_1) {\mathbf{w}_\mathrm{A}}^H \mathbf{n}_\mathrm{A}}_{cross\ term\ 2}. \end{aligned} \tag{4.5}$$

The spatial power spectrum can be obtained by evaluating the magnitude of the output, $|y(u)|$ across different directions in the visible region, i.e., $-1 \leq u \leq 1$. Figure 4.1 compares the contribution of the four terms to the overall spatial spectrum computed using the multiplicative processor for a single snapshot reception of the plane wave source at $u_1 = 0$ in spatially white noise with Signal-to-Noise Ratio in dB given by $\mathrm{SNR}_{dB} = 10\log_{10}\mathrm{SNR} = 40$ dB. The first term in equation (4.5) represents the straight-through source term, i.e., when

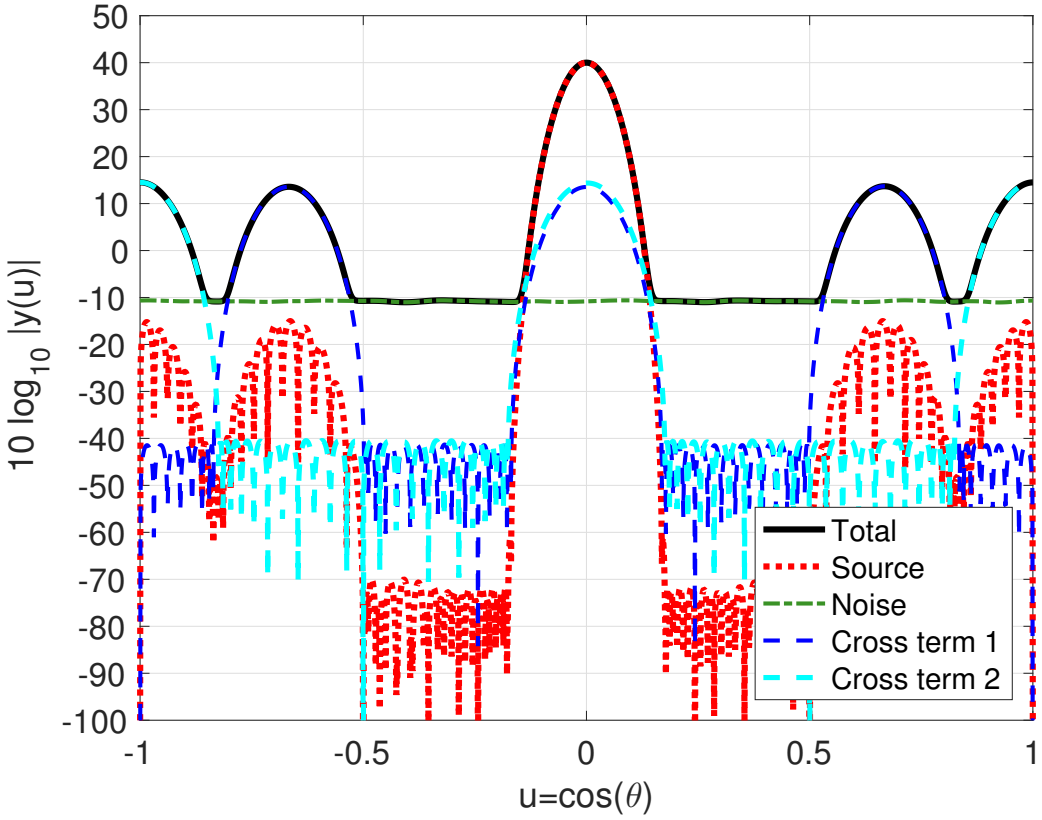

Figure 4.1: The CSA spectrum for source reception at broadside, i.e., $u_1 = 0$ with $\text{SNR}_{dB} = 40$ dB, denoted by *black* dashed line. The colored lines represent the contribution of the individual terms described in the signal model.

both the subarrays process the the signal component. This can be easily predicted by the multiplicative CSA beampattern evaluated at $u_1 = 0$. Figure 4.2 (a) shows the magnitude of the multiplicative beampattern evaluated for $u_1 = 0$ for the given CSA design. Both the subarrays make use of Dolph-Chebychev weights with -110 dB sidelobe levels. The second term in equation (4.5) corresponds to the straight-through noise term, i.e., when both the subarrays process the noise component. The output consists of shared and non-shared sensor terms, i.e.,

$$\mathbf{w}_{\mathrm{A}}{}^{H}\mathbf{n}_{\mathrm{A}}\mathbf{n}_{\mathrm{B}}{}^{H}\mathbf{w}_{\mathrm{B}} = \sum_{i} \mathrm{w}_{A,i}^{*}\mathrm{w}_{B,i}|\mathrm{n}_i|^2 + \sum_{i\neq j}\sum_{j} \mathrm{w}_{A,i}^{*}\mathrm{w}_{B,j}\mathrm{n}_i^{*}\mathrm{n}_j. \tag{4.6}$$

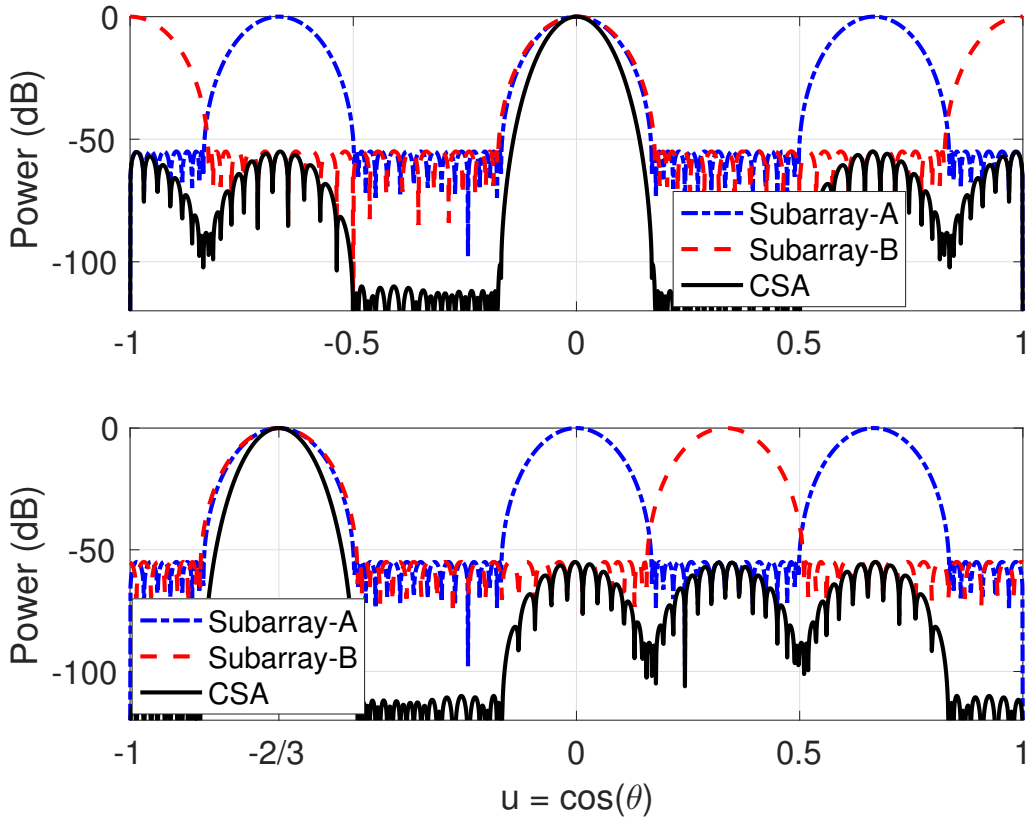

Figure 4.2: CSA multiplicative beampattern evaluated at direction $u_1 = 0$ for the designed subarrays as shown in Figure 3.3. The subarray beampatterns are plotted on a $10\log_{10}$ scale. The subarrays are shaded with Dolph-Chebychev windows with -110 dB sidelobe levels.

The last two terms in equation (4.5) are called *source-noise* cross terms. These are highest when the two subarray beamformers are steered to direction u_c,

$$u_c = \left\{ u_1 \pm \frac{i\lambda}{Md}; u_1 \pm \frac{i\lambda}{Nd} \right\} \qquad \forall i \geq 0, i \in \mathbb{Z}. \tag{4.7}$$

u_c are the locations of the source-noise cross term peaks in the visible spectrum, i.e., for $-1 \leq u_c \leq 1$. The grating lobe of one of the subarrays aligns perfectly with the source location u_1, passing the signal component through the output of the beamformer with unity gain. The noise is processed through the output of the other subarray. Figure 4.2 (b)

illustrates the individual beampatterns of the CSA subarrays steered to $u_c = u_1 - \lambda/Nd$, using the coprime pair $(M, N) = (2, 3)$ and $d = \lambda/2$. The grating lobe of subarray-A aligns perfectly with the source location at $u_1 = 0$. The next section analyzes the effect of averaging the output of the multiplicative processor over multiple snapshots.

4.2 Analysis of Cross terms

Figure 4.3 compares the individual contributions of the four terms described in equation (4.5) to the received output power using multiplicative processing of the 32 sensor CSA design. The output power is computed at the location of the source-noise cross term peaks, specifically, $u_c = u_1 - \lambda/Nd$. The comparison is done as a function of SNR, since SNR $= \sigma_1^2$ (assuming unit noise power, $\sigma_n^2 = 1$). For very high SNR ($\sigma_1^2 >> \sigma_n^2$), the source-noise cross terms are buried beneath the peak sidelobe of the multiplicative beampattern designed for the given CSA.

4.2.1 Noise-noise cross terms

When the signal power is much lower than the noise power (i.e., $\sigma_1^2 << \sigma_n^2$), the output power at u_c, obtained using the multiplicative processor can be predicted by the straight-through noise terms as shown in equation (4.6). The output of the multiplicative processor is a product of two dependent complex Gaussian random variables (since the output consists of shared and non-shared sensor terms)

$$\begin{aligned} y_{\mathrm{A}} &\sim \mathcal{CN}(0, \sigma_n^2 {\mathbf{w}_{\mathrm{A}}}^H \mathbf{w}_{\mathrm{A}}) \\ y_{\mathrm{B}} &\sim \mathcal{CN}(0, \sigma_n^2 {\mathbf{w}_{\mathrm{B}}}^H \mathbf{w}_{\mathrm{B}}). \end{aligned} \tag{4.8}$$

The received noise power $|y| = |y_{\mathrm{A}} y_{\mathrm{B}}^*|$, follows the distribution of the product of two dependent Rayleigh random variables [39]. Using the fact that $|y_A|$ and $|y_B|$ are correlated

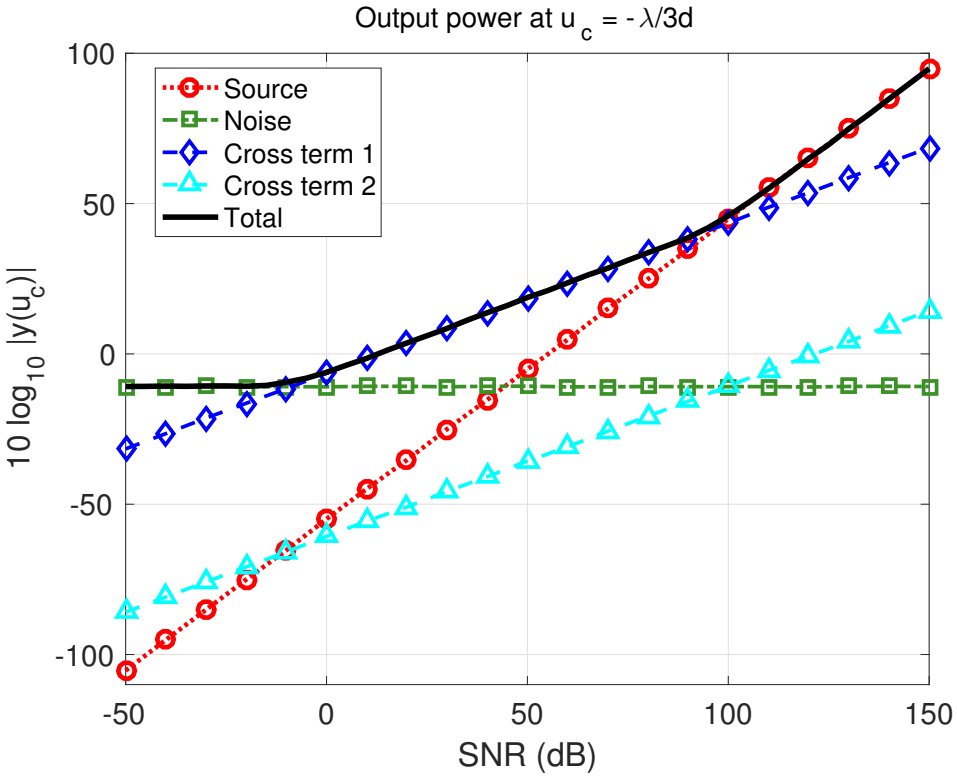

Figure 4.3: Comparison of the output power at $u_c = -\lambda/3d$, the solid line corresponds to the spectral levels obtained using the CSA. The contribution of the individual terms is compared for a range of SNR values in dB.

Rayleigh random variables, with correlation coefficient, ρ given by,

$$\rho = \frac{\sum\limits_{i=shared} \mathrm{w}_{A,i}^{*} \mathrm{w}_{B,i}}{\sqrt{(\mathbf{w}_{\mathrm{A}}{}^{H}\mathbf{w}_{\mathrm{A}})(\mathbf{w}_{\mathrm{B}}{}^{H}\mathbf{w}_{\mathrm{B}})}}. \tag{4.9}$$

The output $|y|$ follows the distribution of the product of two dependent Rayleigh random variables,

$$f(|y|) = \frac{4|y|}{\sigma_a^2\sigma_b^2(1-\rho^2)} \cdot I_0\Big(\frac{2|y||\rho|}{\sigma_a\sigma_b(1-\rho^2)}\Big) \cdot K_0\Big(\frac{2|y|}{\sigma_a\sigma_b(1-\rho^2)}\Big) \tag{4.10}$$

where $I_0(\cdot)$ and $K_0(\cdot)$ are the zeroth order modified Bessel functions of the first and second kind, respectively, and σ_a^2 and σ_b^2 are the variances at the outputs of the subarray-A and

subarray-B, respectively. The expectation of the pdf (4.10) using the required correlation coefficient provides an estimate of the output power at the first snapshot [38]. The output of the multiplicative processor averaged over K snapshots can be given by,

$$y_{\mathrm{K}}(u) = \frac{1}{K}\sum_{k=0}^{K-1} y(u,k). \tag{4.11}$$

The output at the K^{th} snapshot consists of the sum of chi squared random variables (shared sensor terms) and the sum of the product of two uncorrelated complex Gaussian random variables (non-shared sensor terms). These are also called as the *noise-noise* cross terms. By applying the law of large numbers, the non-shared sensor term converges in distribution to a zero mean complex Gaussian random variable with the variance decreasing as a function of $1/K$. Hence, for a sufficient K large (or theoretically, as $K \to \infty$) the output of the CSA at the K^{th} snapshot is mainly dictated by the shared sensor terms i.e., y_K converges in distribution to a Chi-squared random variable. Hence the magnitude of the averaged output at the K^{th} snapshot is defined as

$$FNP = \lim_{K\to\infty} E[|y_K|] = \sigma_n^2 \left| \sum_{i=shared} \mathrm{w}_{A,i}^{*} \mathrm{w}_{B,i} \right|. \tag{4.12}$$

This quantity is referred to as the Final Noise Power (FNP).

4.2.2 Source-noise cross terms

For high SNR ($\sigma_1^2 > \sigma_n^2$), the multiplicative spectra at u_c is dominated by the contribution of the source-noise cross term, i.e., when the source signal is processed through the output

of subarray-A and the noise through the output of subarray-B,

$$\begin{aligned} y_{\mathrm{A}}(u_c) &\sim \mathcal{CN}(0, \sigma_1^2) \\ y_{\mathrm{B}}(u_c) &\sim \mathcal{CN}(0, \sigma_n^2 {\mathbf{w}_{\mathrm{B}}}^H \mathbf{w}_{\mathrm{B}}). \end{aligned} \tag{4.13}$$

The output of the multiplicative processor at u_c for a single snapshot is a product of two independent complex Gaussian random variables, also known as a complex double Gaussian random variable [40]. Since the signal and noise components are assumed to be independent of each other, the output power is obtained by taking the magnitude follows the distribution of the product of two independent Rayleigh random variables, $|y_1(u_c)| = |y_A(u_c)|.|y_B(u_c)|$,

$$\begin{aligned} E[|y_1(u_c)|] &= E[|y_A(u_c)|]E[|y_B(u_c)|], \\ &= \sqrt{\frac{\pi\sigma_1^2}{4}}\sqrt{\frac{\pi\sigma_n^2 {\mathbf{w}_{\mathrm{B}}}^H \mathbf{w}_{\mathrm{B}}}{4}}, \end{aligned} \tag{4.14}$$

$$E[|y_1(u_c)|] = \frac{\pi}{4}\sigma_1\sigma_n\sqrt{{\mathbf{w}_{\mathrm{B}}}^H \mathbf{w}_{\mathrm{B}}}. \tag{4.15}$$

As the output is averaged over multiple snapshots, each $y(u_c, k)$ is a product of two independent complex Gaussian random variables and since each snapshot is independent, the law of large numbers suggests that the sum of the product of two independent complex Gaussian random variables for large K approaches a complex Gaussian random variable. As the real and imaginary parts of the sum will follow the sample distribution of a Gaussian random variable, i.e., as $K \to \infty$, $y_K(u_c) \sim \mathcal{CN}(0, \sigma_1^2\sigma_n^2 {\mathbf{w}_{\mathrm{B}}}^H \mathbf{w}_{\mathrm{B}}/K)$. The output power at the K^{th} snapshot can be estimated as

$$E[|y_K(u_c)|] = \sqrt{\frac{\pi}{K}}\frac{\sigma_1\sigma_n\sqrt{{\mathbf{w}_{\mathrm{B}}}^H \mathbf{w}_{\mathrm{B}}}}{2}. \tag{4.16}$$

Combining equations (4.15) and (4.16), a relationship for the decay of the cross terms due to averaging can be obtained,

$$\frac{E[|y_1(u_c)|]}{E[|y_K(u_c)|]} = \frac{\sqrt{\pi K}}{2} \tag{4.17}$$

Taking $10\log_{10}$ on either side of the equation shown above and using the fact that $10\log_{10}\frac{\sqrt{\pi}}{2} = -0.5246$. For large values of K,

$$10\log_{10} E[|y_1|] - 10\log_{10} E[|y_K|] \approx 5\log_{10} K \tag{4.18}$$

The source-noise cross terms decay with averaging over snapshots by a factor of $5\log_{10} K$ dB, i.e., the cross term peaks decay at a rate of 5 dB per decade of snapshots the output is averaged over. When the source-noise cross terms attain a significant amount of decay (i.e., after sufficient snapshot averaging), the output power at u_c approaches the final noise power value predicted by equation (4.12). We define the ratio $CTNR$ (Cross Term-to-Noise Ratio) as a function of the number of snapshots averaged,

$$CTNR(k) = \frac{E[|y_k(u_c)|]|}{FNP}. \tag{4.19}$$

In Figure 4.4, the solid colored lines indicate the ratio of the total power obtained using the multiplicative CSA processor to the final noise power as a function of the number of snapshots averaged obtained using simulated signals of varied signal strengths, the result is averaged over 1,000 Monte Carlo trials. The dashed lines indicate the CTNR using analytical predictions of the source-noise cross term decay showing excellent agreement with the simulated results.

As a final evaluation step, let us compare the cumulative average of the scanned response as a function of the number of snapshots averaged. Figure 4.5 uses an $\text{SNR}_{dB} = 40$ dB and the average is performed over 10^6 number of snapshots. There is a clear evidence of the presence of source-noise cross-terms at endfire as predicted by the analysis done before.

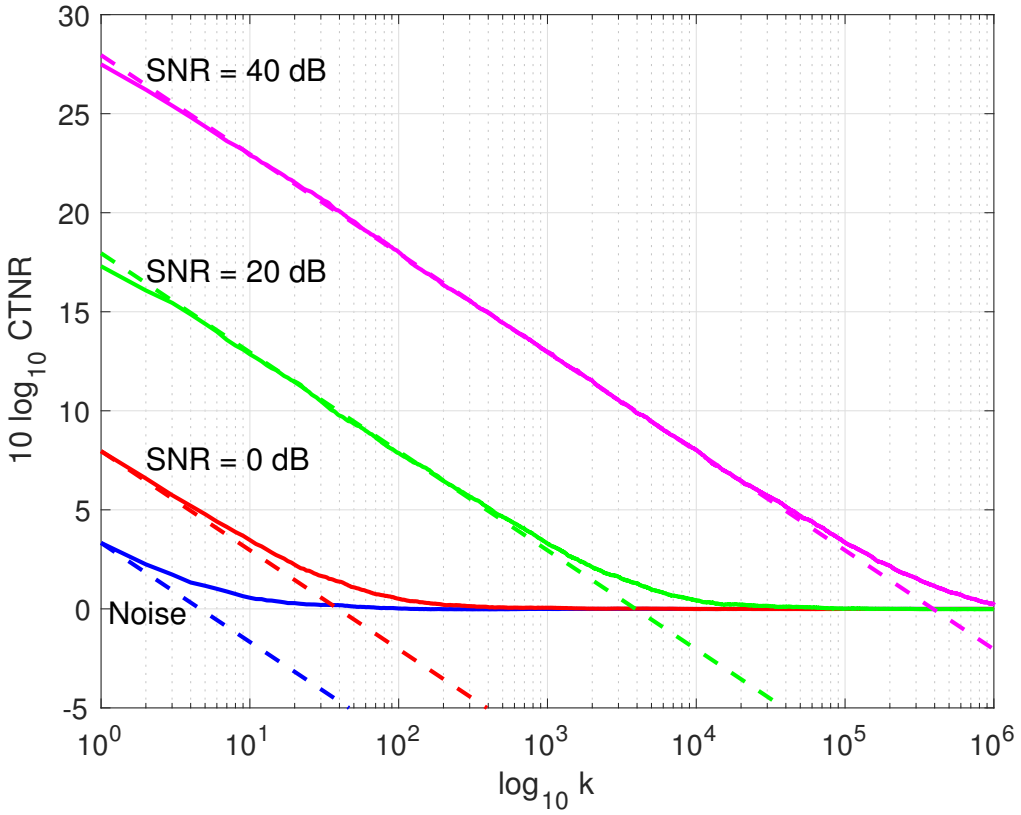

Figure 4.4: The figure illustrates the decay observed at the cross term peaks as a function of snapshot averaging. The solid colored lines indicate the ratio of the total power obtained using the multiplicative CSA processor to the final noise power using simulated signals of various SNR values. The dashed lines represent the CTNR using the analytical predictions.

With averaging, since the signal and noise are assumed to uncorrelated a significant decay is observed as the number of snapshots averaged increases. Using Figure 4.4 the CTNR computed for the $\text{SNR}_{dB} = 40$ dB at the 10^6 snapshot reaches to the final noise power (FNP). This is in agreement with the cumulative average scanned response. Figure 4.6 compares the first and last snapshot slices of the cumulative response indicating the overall decrease from the first to the last snapshot.

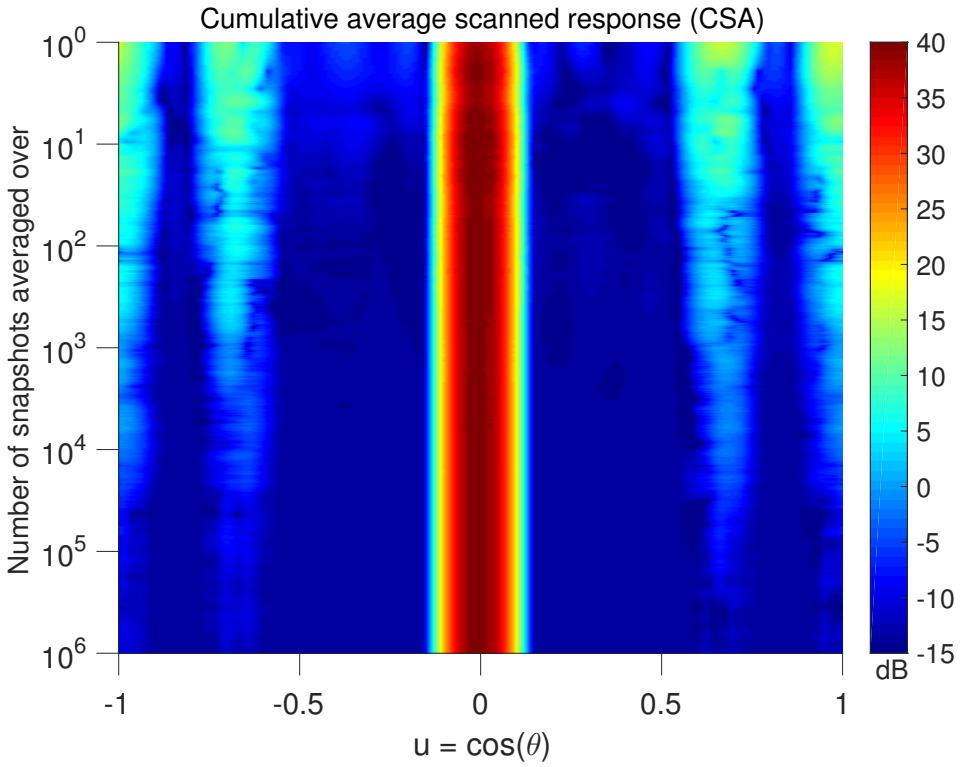

Figure 4.5: Cumulative average scanned response of the formulated signal model using a single source in noise with an SNR=40 dB, the scanned response is averaged over 10^6 snapshots, illustrating the decay observed at the cross terms peaks.

4.2.3 Source-source cross terms

Consider processing two sources with directional cosines u_1 and u_2 using the CSA. Cross terms observed at the output of the multiplicative processor occur when one source falls in the grating lobe of subarray-A and the other source appears in the grating lobe of subarray-B, i.e., when the two sources are the difference $|u_2 - u_1| = |\lambda/Md - \lambda/Nd|$ apart in u space, the cross term puts maximum energy outside the bandwidth of the source signal. These cross terms are known as *source-source* cross terms. Let $s_2 \sim \mathcal{CN}(0, \sigma_2^2)$ be the signal component of the second source, the output of the multiplicative processor at the peak of these cross terms, u_{sc} is dominated by the term,

$$y(u_{sc}) = s_1 s_2^* B_{A,u_{sc}}(u_1) B_{B,u_{sc}}^*(u_2) \tag{4.20}$$

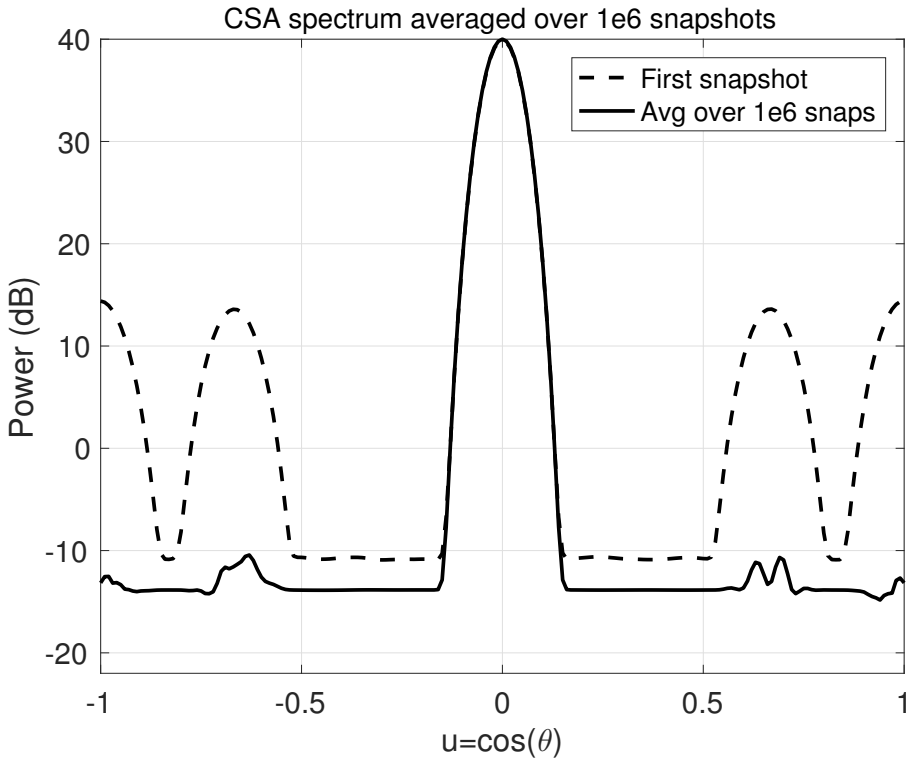

Figure 4.6: The averaged scanned response at the first snapshot and the 10^6 snapshot is compared showing the overall decay observed at the cross term peaks.

If s_1 and s_2 are perfectly correlated random variables, the source-source cross terms will exist in the multiplicative CSA spectrum and will not decay. Whereas, if s_1 and s_2 are uncorrelated, the source-source cross terms will also decay at a rate of $5 \log_{10} K$. As an illustration consider the signal model consisting of two sources in noise, the output of the multiplicative processor will now consist of 9 terms, 2 straight-through source terms, 1 noise only term, 2 source-source cross terms and 4 source-noise cross terms.

Figure 4.7 shows the cumulative scanned response computed for a signal model using 2 source in the presence of spatially white noise, $\text{SNR}_{dB} = 10$ dB for both sources and the average is computed using $1,000$ snapshots. The presence of the source-noise and source-source cross terms is evident in the plot and the decay is observed since the two sources are uncorrelated. For the averaged result refer to Figure 4.8 which compares the first and last

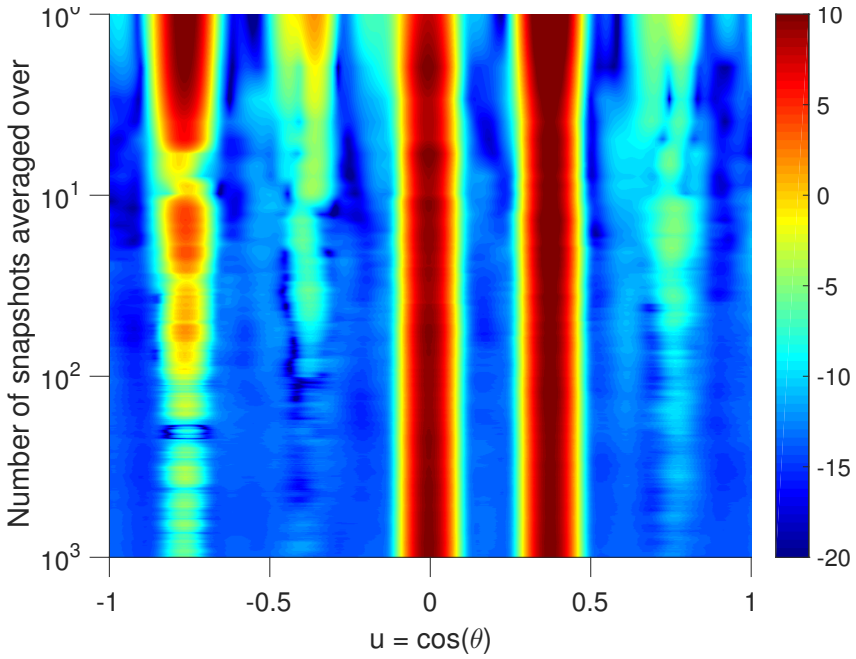

Figure 4.7: Simulation of two sources in noise averaged over 1,000 snapshots, illustrating the decay observed at the locations of the signal and noise cross terms. $\text{SNR}_{dB} = 10$ dB (both sources).

snapshot of the cumulative response, indicating the overall decay of the cross terms.

The CSA designs are more susceptible to the generation of source-source cross terms as shall be observed in the next chapter. As both the CSA subarrays are undersampled which produces grating lobes, although they do not intersect, but when one source aligns with the grating lobe of one subarray and the second source aligns with the grating lobe of the other subarray, the output received at the beamformer steered to the cross term peak location will observe loud arrivals at these locations in the estimated spatial spectrum. This however is not much of a huge concern for the NA designs since they employ the use of a single undersampled subarray, the cross terms will put maximum energy outside the bandwidth of the source when one source aligns perfectly with the grating lobe of the outer subarray (aliased) and the other source falls in the mainlobe (wider mainlobe due to reduced aperture) of the inner subarray. The possibility of such a situation occurring is quite low [41].

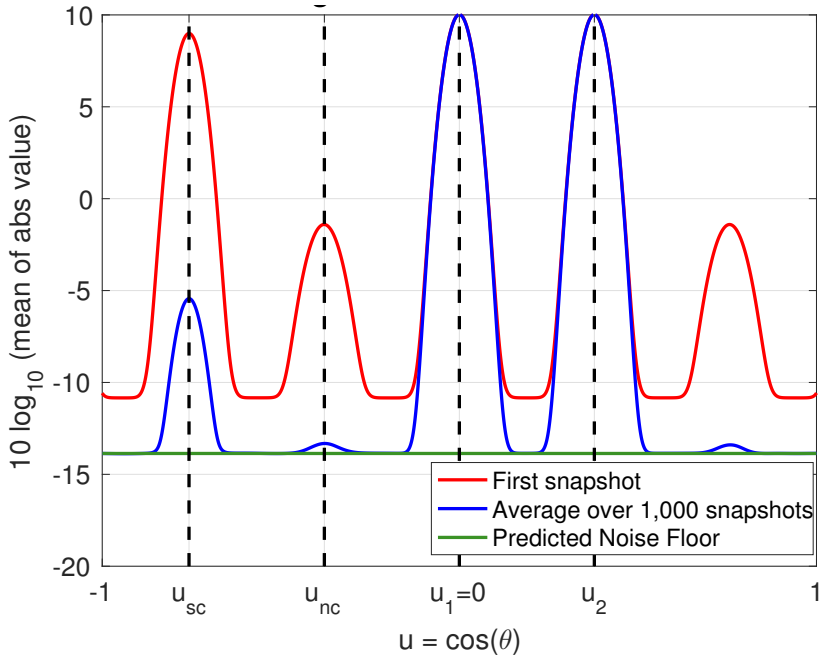

Figure 4.8: This figure illustrates that with averaging over snapshots the noise cross terms and signal cross terms approach the final noise power predicted by the product of the weights for the shared sensors between the two subarrays.

4.3 When does the min processor fail to eliminate the ambiguity due to undersampling?

The min processor combines the spectral estimates observed by the two subarrays independently by taking the minimum at each directional cosine. Since the CSA makes use of two undersampled subarrays the spectral estimates obtained by the two subarrays will consist of the aliased copies of the source signal centered at the two distinct grating lobe locations. Lets consider that the source signal is spatially bandlimited, i.e., it spans over a discrete set of directional cosine values. The individual CSA subarrays will produce a spectral estimate that consists of this bandlimited source signal centered at the grating lobe locations. There exists a possibility that these aliased copies might overlap and the output of the min processor at the overlap locations would not be able to eliminate these ambiguous terms.

Since the NA design makes use of one less undersampled subarray, the possibility of such

an overlap is quite rare. Although there does exist a possibility if the source signal sensed by the inner subarray (non-aliased, but wider mainlobe) has a spread that overlaps with the copies of the source signal at the grating lobe locations predicted by the outer subarray (aliased).

4.4 Summary

The spatial spectrum computed by a multiplicative processor using a coprime array introduces loud arrivals/peaks due to the generation of cross terms at the output when compared to a conventional ULA processor. For high values of SNR, the cross term peaks appear to be a dominant factor in the multiplicative spectrum, which requires averaging the output over a large number of snapshots in order to mitigate their effect. Analytical and simulated results presented in this chapter are conclusive and show that the cross terms decay at a rate of 5 dB per decade of snapshots averaged. Moreover, in cases where the two sources are correlated these cross terms do not decay with any amount of averaging. The chapter also identifies the case when the min processor is used to estimate the spectrum for spatially bandlimited signals, there exists a possibility that it will not be able to eliminate the ambiguity produced by the undersampled subarray(s) of the NA or CSA.

Chapter 5: Analysis of the Elba data using CSA and NA

The previous chapter highlighted the issue of cross terms arising at the output of a multiplicative processor using a Gaussian signal model and derived the analytical cross term decay at the location of the cross term peaks in the estimated spatial spectrum. The cross term decay rate was verified using a numerical simulation. The analysis also identified the worst case scenario when two correlated sources are present, demonstrating that the source-source cross terms generated at the output of the multiplicative processor do not decay with averaging in this case. This chapter analyzes the spatial spectrum estimates of the Elba data using the CSA/NA beamformer designs as defined in Table 3.1. Section 5.1 estimates the spatial spectrum at the center frequency of the RM2 signal, i.e., at 335 Hz, using the multiplicative processors and addresses the issue of cross-terms. Section 5.2 provides the results of estimating the spatial spectrum for the RM2 signal at the center frequency using min processing of the data. Section 5.3 compares the wavenumber-frequency plots to provide a summarized view for each of the processors analyzing the spectrum for the Elba RM2 data.

5.1 CSA/NA multiplicative processing of the Elba data

The CSA and NA designs provide a multiplicative beam pattern that achieves the peak sidelobe level of -55 dB and attains equal resolution as the Elba ULA using a conventional beamformer with peak sidelobes of -103 dB. Since our goal here is to achieve the spatial Power Spectral Density (PSD) we will make use of the S-2 based normalization of the subarray weights (refer to appendix B for details about normalizing for true PSD). Figure 5.1 shows the cumulative average of the spatial spectrum for the RM2 source signal at the center frequency of 335 Hz, computed by the multiplicative processor using the CSA design

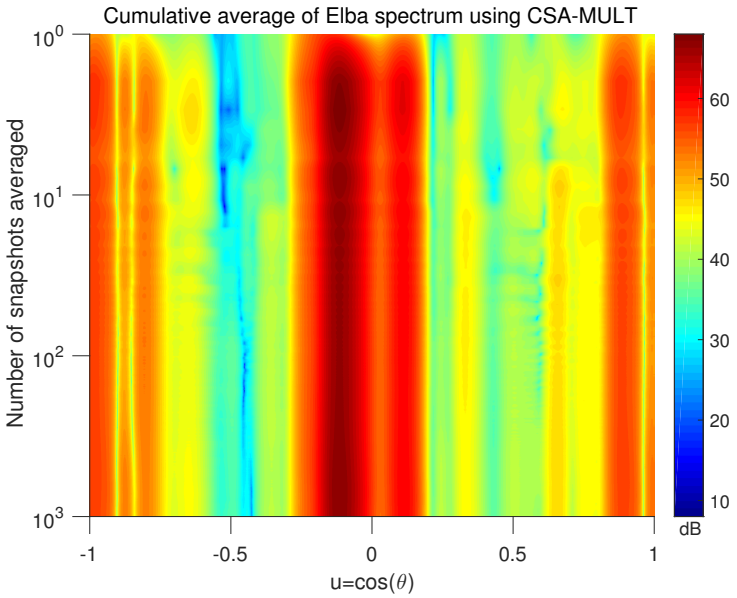

(a) CSA-Multiplicative processor

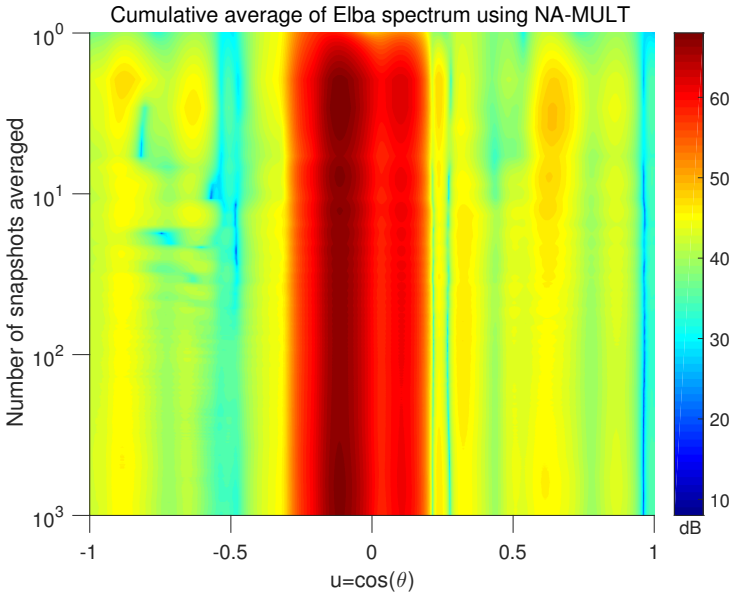

(b) NA-Multiplicative processor

Figure 5.1: Cumulative average of the spatial spectrum computed using a multiplicative processor for the 335 Hz reception in the Elba data. The multiplicative processors make use of, (a) CSA design with coprime factors $(M, N) = (2, 3)$ and, (b) NA design using $(Q, c) = (3, 8)$. The CSA response contains high energy arrivals around endfire. The cumulative average is performed for $1,000$ snapshots of Elba data.

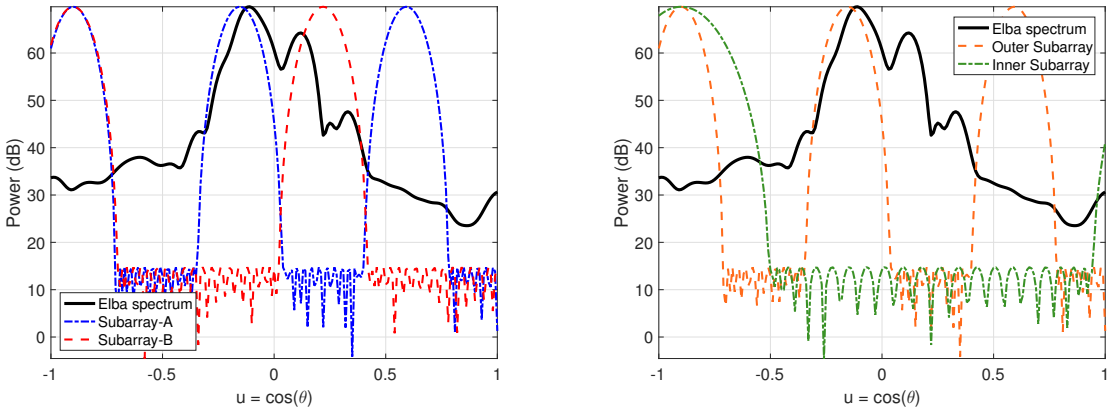

(a) CSA-mult (b) NA-mult

Figure 5.2: Subarray beampatterns of the CSA and NA designs overlaid on top of the Elba spectrum computed using the conventional ULA illustrating the generation of cross terms due to the leakage observed through the grating lobes.

with coprime factors, $(M, N) = (2, 3)$ and the NA design with parameters $(Q, c) = (3, 8)$. Although the plots reveal the general nature of the source signal around broadside, the response from the CSA consists of high energy arrivals around endfire that do not decay with averaging. It can be shown that the output at the endfire locations consists of coherent cross terms.

To illustrate the behavior of cross terms at the output of multiplicative processor, consider Figure 5.2 which shows the subarray beam patterns of the designed CSA and NA steered to one of the locations of the loud arrivals overlaid on top of the Elba spectrum computed using the ULA. The high energy endfire arrivals in the multiplicative spectra are associated with the leakage observed through the grating lobes of the CSA and NA, since they align perfectly with the source signal at broadside. Figure 5.2 also shows lower endfire arrivals observed by the NA since it makes use of one less undersampled subarray. These arrivals do not seem to reduce with averaging. By the analysis done in chapter 4, the cross terms (if uncorrelated) must decay at a rate of 5 dB/decade of snapshots averaged, i.e., the total decay if the cross terms are produced by uncorrelated sources should be down by -15 dB from the first snapshot. Clearly, that is not the case.

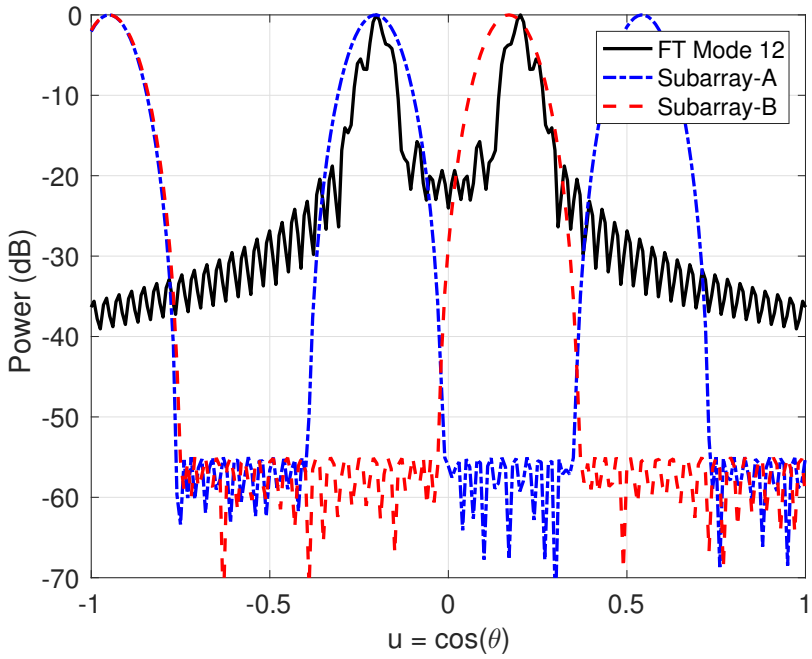

Figure 5.3: Fourier transform of the modeshape of mode 12 shown in bold-black overlaid on top of the subarray beampatterns of the CSA steered to endfire illustrating the effect of coherent cross terms.

To provide more insight into why the cross terms do not average out, consider a model for the propagation of sound in a shallow water column. The sound pressure observed by a receiver in a waveguide can be represented using a weighted sum of the normal modes [37]. Appendix A provides a short description of the normal modes of propagation in the shallow waters at the Elba site [42]. Figure 5.3 shows the Fourier transform of the modeshape of mode number 12 overlaid on top of the individual subarray beampatterns of the CSA steered to a direction around endfire. The two grating lobes align perfectly with the mainlobes of the Fourier transform of the modeshape. Since a single mode is coherent with itself, the output of the multiplicative processor at the endfire direction will consist of coherent cross terms which do not decay with averaging in time. One motivation for considering the nested configuration is that the cross terms are less of a problem for NA designs because only one of the subarrays has a grating lobe, i.e., the maximum cross term for the NA design is

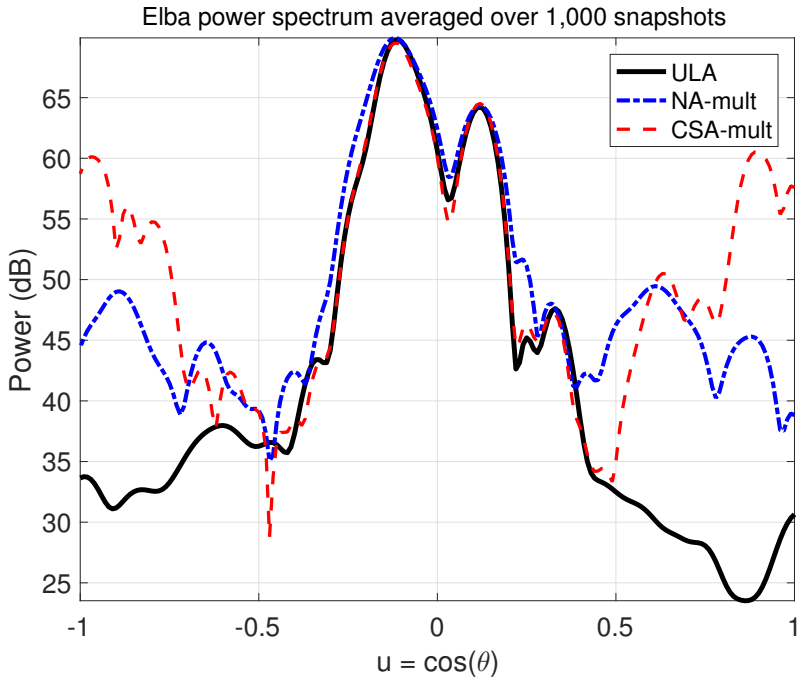

Figure 5.4: Multiplicative Elba power spectrum computed using the designed CSA and NA. The spectrum is averaged over 1,000 snapshots.

smaller than for the CSA design.

The averaged spatial spectrum for the reception of the RM2 source signal evaluated at the center frequency of 335 Hz is shown in Figure 5.4. The response from the multiplicative processors provide endfire arrivals that are higher by approximately $20-25$ dB for the CSA and $10-15$ dB for the NA when compared to the ULA. These are associated with the coherent cross terms due to the modal propagation in the Elba environment.

5.2 CSA/NA min processing of the Elba data

The output of the min processor, $\mathbf{y}_{min}$ can be obtained by taking a minimum of the two subarray outputs, i.e.,

$$\mathbf{y}_{min} = \min(|y_{\mathrm{A}}|^2, |y_{\mathrm{B}}|^2). \tag{5.1}$$

Since the CSA makes use of undersampled subarrays, the individual response of the two

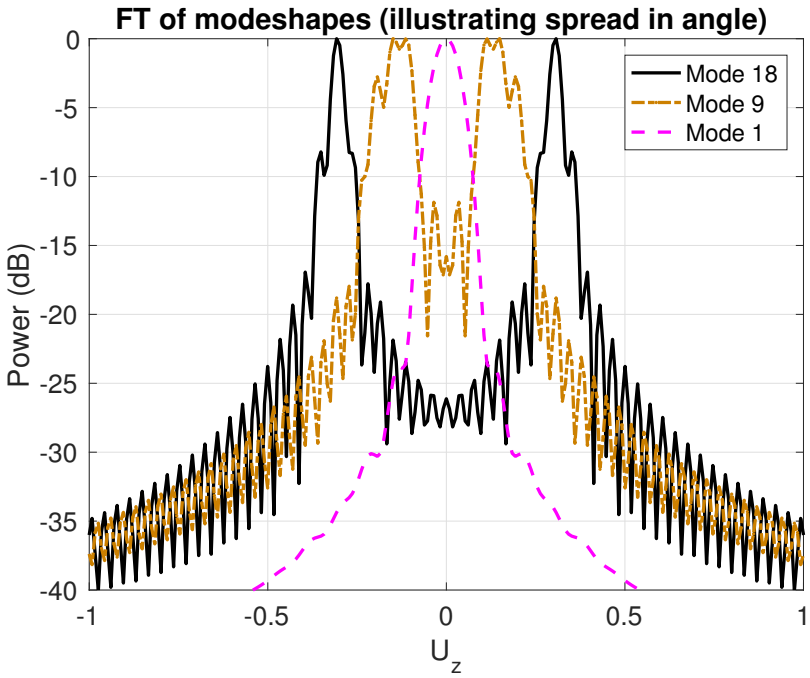

Figure 5.5: Comparison of the Fourier transform of the modeshapes corresponding to mode numbers 1, 9 and 18. This provides with a raw estimate of the signal spread in angle or directional cosine.

subarrays will consist of copies of the source signal to be present/centered at the corresponding grating lobe locations. Although, the coprimality of the undersampling factors ensures distinct grating lobe locations, the CSA-min processor will be successful in eliminating the ambiguity as long as the aliased copies of source signal do not overlap. The NA-min processor will eliminate the ambiguity produced by the outer subarray as long as the copies of the source signal in the response of the outer subarray does not overlap with the source signal sensed by the non-aliased inner subarray. We can estimate the spread of the source signal over a discrete set of directional cosines by looking at the Fourier transform of the modeshape corresponding to the last mode number (refer Appendix A). In this case, the KRAKEN normal mode program provides the shapes for 18 propagating modes. Figure 5.5 looks at a selected few modeshapes by computing their Fourier transforms over the directional cosine. The source signal spread is estimated to be in the range $-0.3 \leq u \leq 0.3$,

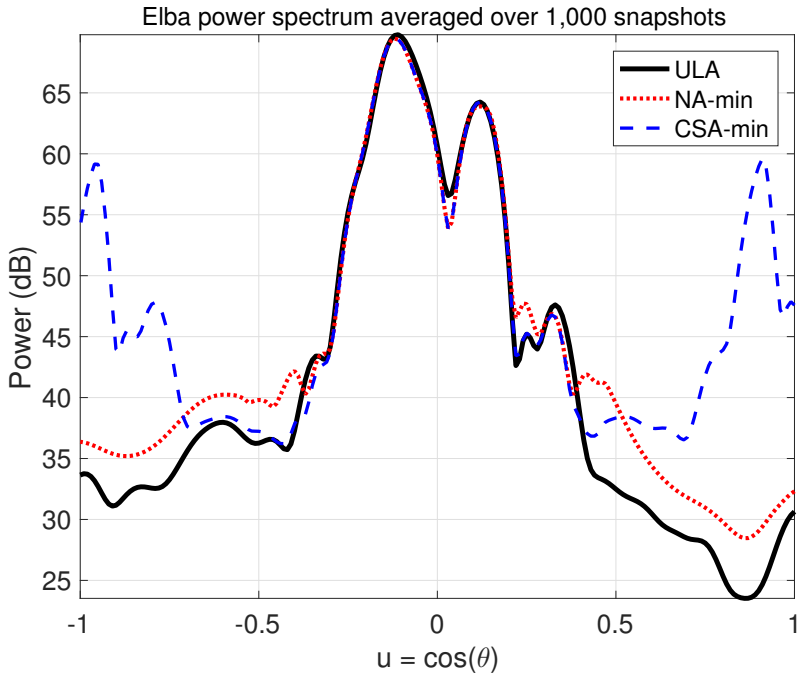

Figure 5.6: Averaged power spectrum of the 335 Hz reception of the Elba data evaluated for the CSA and NA designs using min processors. The averaged ULA spectrum (shown in bold-black) is computed using a conventional processor.

consistent with the Elba spectrum computed using the ULA.

Figure 5.6 shows the average power spectrum of the Elba data at 335 Hz processed using min processors for the CSA and NA. The response from the two processing techniques applied to the CSA and NA designs are compared to the response obtained from conventional processing of the 48-sensor Elba ULA. The spectrum is averaged in time over $1,000$ snapshots. The response from the CSA-min processor fails to eliminate the overlapping copies of the source signal present at the grating lobe locations. The NA-min processor provides with a spatial spectrum that is similar to the ULA around broadside. The output of the NA-min processor outside the bandwidth of the source signal is controlled by the inner subarray. The spectral levels at these locations are higher by approximately $3-4$ dB. This can be explained by recalling that the inner subarray was restricted to span half the aperture of the ULA, i.e., the inner subarray makes use of a wider mainlobe allowing for

more signals and/or noise to leak through to the output.

5.3 Comparison of the $k-\Omega$ spectra using CSA/NA multiplicative and min processors

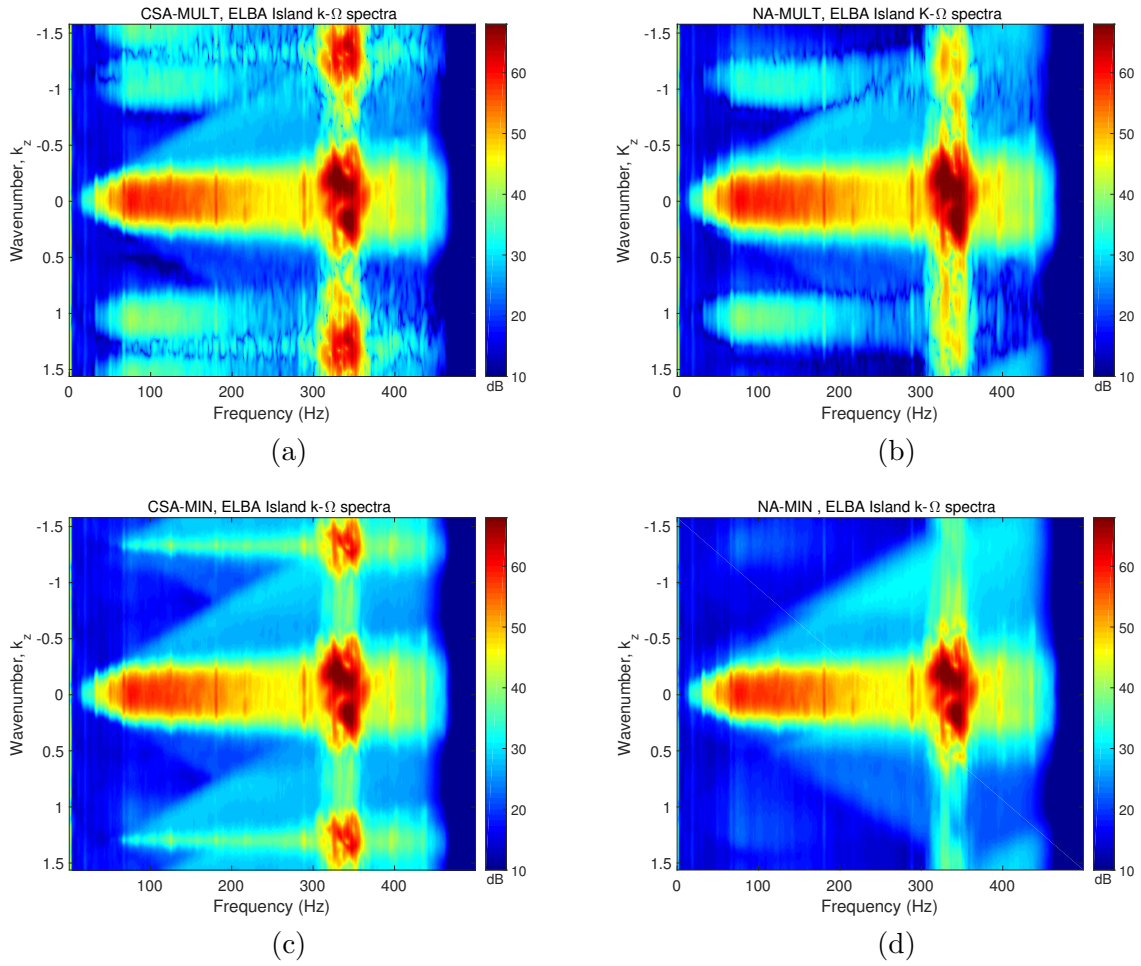

Figure 5.7: Comparison of the wavenumber-frequency $(k-\Omega)$ plots for the Elba data with the source signal RM2 transmitting a pseudorandom sequence with center frequency and bandwidth of 335 ± 15 Hz computed using (a) CSA-MULT, (b) NA-MIN, (c) CSA-MULT, and (d) NA-MIN.

Figure 5.7 compares the wavenumber-frequency $(k-\Omega)$ spectrum obtained from multiplicative processing and min processing of the designed CSA and NA. The spectrum

estimated using the multiplicative processors reveal the effect of cross terms. The cross terms move out of the visible region as the frequency is reduced. The spectrum estimate obtained using the CSA-min processor illustrates the overlap between the aliased copies of the signal at the grating lobe locations. The NA-MIN processor provides with a $k - \Omega$ spectrum (shown in Figure 5.7 (d)) that is comparable to the ULA spectrum.

The Mean Squared Error (MSE) is computed as mean squared error of the difference in the spectral levels of the estimated spatial spectrum obtained using the designed CSA and NA when compared to the spectrum computed using the conventional processor. Figure 5.8 shows the MSE computed as a function of the temporal frequency. Due to the dynamic range of the signal powers in the Elba data the squared error at each spatial frequency is comparatively high providing with similar MSE profiles. The multiplicative processors provide with a higher MSE than the min processors.

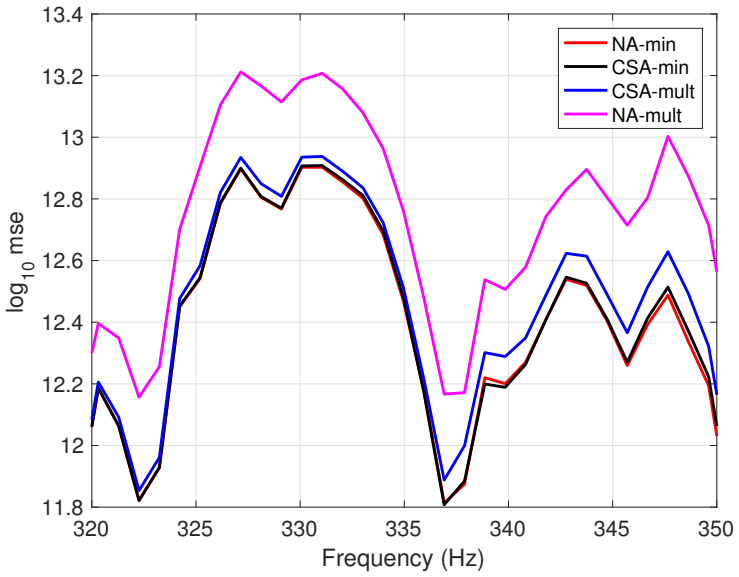

Figure 5.8: Comparison of the squared error of the spatial power spectral density obtained by the CSA and NA when compared to the ULA. The average is taken over the spatial frequencies and computed for the center frequency and bandwidth of the source signal 335 Hz $\pm$15 Hz.

5.4 Summary

This chapter analyzed the performance of each of the designed CSA and NA beamformers in estimating the spatial power spectrum of the Elba data set corresponding to the RM2 source signal. The estimated spatial power spectrum for the receptions of the RM2 signal at the center frequency of 335 Hz was analyzed. Unexpected loud arrivals at endfire hinted towards the possibility of cross terms at the output corrupting the spectrum. To analyze that further, the beam patterns overlaid on top of the true Elba spectrum (as sensed by the ULA) provided a strong indication of the generation of source-source cross terms, as seen in the narrowband simulations. To further support the evidence a normal mode model shows that as even a single mode is coherent with itself, the source-source cross terms generated at the output are highly correlated and do not decay with averaging. The CSA and NA using multiplicative processors provided an averaged spatial spectra with endfire arrivals approximately 30 dB and 20 dB higher than the ULA, respectively.

The KRAKEN normal mode program provided with only 18 propagating modes which span only a small subset of the angle space. The min processor applied to the NA design provided with the best spectral estimate making most out of the spatially bandlimited signal. The CSA-min however fails to get rid of the ambiguity as there was significant overlap between the aliased copies of the source signal.

Chapter 6: Conclusion

6.1 Summary

This thesis approached the problem of designing coprime and nested arrays that would provide with suitable sensor savings compared to the 48−sensor Elba ULA. The Elba Island data was first analyzed using a conventional ULA beamformer to obtain clear understanding of the design requirements. The beampattern parameters (resolution and peak sidelobe level) of the ULA were used as a benchmark to compare the beam patterns obtained by applying multiplicative and MIN processing to the individual subarrays of the CSA and NA. The chosen CSA and NA designs require 32 sensors, i.e., a savings of 33% in the cost and maintenance of the sensors. The CSA design used coprime factors, $(M, N) = (2, 3)$ where the subarrays are extended to span the aperture of the ULA. The NA design made use of the design parameters $(Q, c) = (3, 8)$. All the designs attained the minimum desired peak sidelobe level and had similar resolution.

Cross terms observed at the output of the multiplicative processors were identified to be a cause for concern as they may produce ambiguities in the spatial spectrum. Averaging in time helps to compensate for the effect of incoherent cross terms. The 335 Hz reception of the Elba data was analyzed using multiplicative processing of the designed CSA and NA subarrays. The spectrum was averaged over $1,000$ snapshots. The averaged CSA spectrum consisted of high energy arrivals near endfire, which did not decay. A normal mode model showed that even a single mode is coherent with itself, the output of the multiplicative processors at the endfire direction consisted of cross terms that are highly correlated. The NA performs fairly better since it makes use of one less undersampled subarray. The averaged spectrum computed using the CSA-MIN processor consists of the ambiguities in the spectrum around endfire, as there is significant overlap between copies of the source

signal generated from the two undersampled subarrays. The NA-MIN processor provides with a response that is comparable to the ULA.

6.2 Suggestions for Further Research

This thesis implemented coprime and nested arrays for the Elba ULA using both multiplicative and min processors. Comparison with the conventional processing of the Elba data highlighted significant effects of coherent cross terms. The derivation of the cross term decay relied on the law of large numbers. For an exact analysis, a moment generating function is required to analyze the pdf of the moving average of the complex double Gaussian terms.

The co-array based beamforming approach makes use of the estimated covariance matrix and does not require the multiplication of the beamformed outputs. Also the estimated covariance matrix could be used to analyze the performance of using the linear non-uniform array designed with the coprime and nested design framework by applying adaptive processing techniques. The presence of cross terms in the estimated covariance matrix based approaches needs to be examined.

The estimates of the mode powers obtained using multiplicative processors are similar to the ULA. However it is difficult to retain the correlation structure of these estimated mode powers. Further research could be focused on obtaining the mode powers using the multiplicative processors and analyzing the reconstruction of the power spectrum using correlated and uncorrelated modes.

Appendix A: Normal modes of propagation in a shallow water column

The homogeneous Helmholtz equation described in three dimensions using, $\mathbf{r} = \{r, \phi, z\} \in$ cylindrical coordinate system can be given as [37]

$$\nabla^2 p(\mathbf{r}) + k^2(\mathbf{r}) p(\mathbf{r}) = 0, \tag{A.1}$$

where $k(\mathbf{r}) = \frac{2\pi f}{c(\mathbf{r})}$ acoustic wavenumber. The thesis makes use of a linear array and the equation can be simplified for the two dimensions (range and depth)

$$\frac{1}{r}\frac{\partial}{\partial r}\left(r\ \frac{\partial p}{\partial r}\right) + \rho(z)\frac{\partial}{\partial z}\left(\frac{1}{\rho(z)}\frac{\partial p}{\partial z}\right) + \frac{(2\pi f)^2}{c^2(z)} p = -\frac{\delta(r)\delta(z - z_s)}{2\pi r}, \tag{A.2}$$

where r is the range of the source in meters. ρ and c are the density and sound speed depending only on depth z. The frequency of the propagating signal is given by f in Hertz. Using a technique of separation of variables the modal equation is a classical *Sturm-Liouville* eigenvalue problem [43]. The ideal eigenvalue problem yields an infinite number of solutions (similar to the modes of a vibrating string). Assuming the density and sound speed are real functions of depth z, the depth dependent eigenfunction equation can be given as

$$\frac{d^2}{dz^2}\Psi_m(z) + k_{zm}^2(z)\Psi_m(z) = 0, \tag{A.3}$$

where $\Psi_m(z)$ are the eigenfunctions or *modeshapes* for mode m at depth z. The vertical wavenumber of mode m is given as, $k_{zm}(z) = \sqrt{k^2(z) - k_{rm}^2}$ and k_{rm} is the horizontal wavenumber of mode m. This thesis makes use of the normal modes to study the propagation of sound by modeling the pressure received at a given depth z and range r in an

underwater environment with well specified boundary conditions, sound speed profile, density measurements, description of the point source location in range and depth and the propagation of the narrowband signal (center frequency of the Elba source). The pressure received can be modeled as

$$p(r,z) = \sum_m a_m(r)\Psi_m(z), \tag{A.4}$$

where $a_m(r)$ is the the mode coefficient at range r.

$$a_m(r) = \frac{i}{4\rho(z_s)}\Psi_m(z_s)H_0^{(1)}(k_{rm}r), \tag{A.5}$$

where $H_0^{(1)}$ is the zero-order Hankel function of the first kind. The pressure received at a single point at (z,r) in the bounded space can be given as,

$$p(r,z) = \frac{i}{\rho(z_s)\sqrt{8\pi r}}e^{-i\pi/4}\sum_{m=1}^{\infty}\Psi_m(z_s)\Psi_m(z)H_0^{(1)}(k_{rm}r). \tag{A.6}$$

KRAKEN is a normal mode program that can be used to obtain the solutions of the modal equation [42]. The program provides the user with the modeshapes and mode coefficients using an input environmental file which consists of the parameters required to compute the modal equation as described above. The sound speed profile at the Elba array site is as shown in the left panel of Figure A.1. The modeshapes computed at the Elba VLA site is shown in the right panel of Figure A.1. The point source at 74 m depth from the surface and at 5400 m from the Elba VLA using a 335 narrowband frequency provides with only 18 *propagating* modes. The rest of the modes are *evanescent*, i.e., vertical wavenumbers of these modeshapes are imaginary.

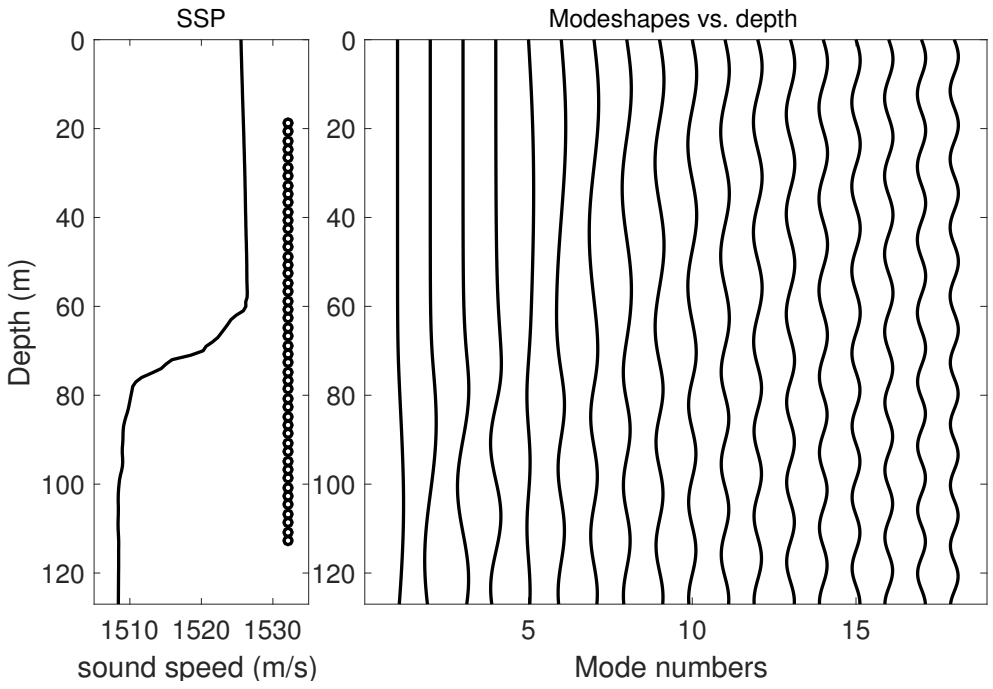

Figure A.1: The left panel indicates the sound speed profile measured during the experiment and the right panel shows the modeshapes corresponding to the 18 modes of propagation of the Elba environment computed using the KARKEN normal mode program.

The vector of pressures measured by an N-element linear array can be modeled as

$$\begin{bmatrix} p(z_1) \\ p(z_2) \\ \vdots \\ p(z_n) \end{bmatrix} = \begin{bmatrix} \psi_1(z_1) & \psi_2(z_1) & \dots & \psi_m(z_1) \\ \psi_1(z_2) & \psi_2(z_2) & \dots & \psi_m(z_2) \\ \vdots & \vdots & \ddots & \vdots \\ \psi_1(z_n) & \psi_2(z_n) & \dots & \psi_m(z_n) \end{bmatrix} \begin{bmatrix} a_1 \\ a_2 \\ \vdots \\ a_m \end{bmatrix} + \begin{bmatrix} n(z_1) \\ n(z_2) \\ \vdots \\ n(z_n) \end{bmatrix}, \tag{A.7}$$

where $\mathbf{n}$ is the observation noise and $z_1, z_2, \dots, z_n$ are the locations of the hydrophones.

Appendix B: Normalizing the weights for PSD estimation

Heinzel et al. suggests normalizing the weights of a spatial filter is done to satisfy one of two constraints [32]:

S-1 - To obtain unity gain in the source direction,

S-2 - To obtain the true Power Spectral Density (PSD).

For most of the thesis, we have made use of the S-1 normalization scheme for its simplicity in design. For example, consider the designed spatial filter for a L-sensor ULA, $\mathbf{w}$. The S-1 normalization is achieved by normalizing the spatial filter/ weight vector by its L1 norm,

$$(\textbf{S-1}) \qquad \frac{\mathbf{w}}{||\mathbf{w}||_1} = \frac{\mathbf{w}}{\sum_{i=1}^{L} |\mathrm{w(i)}|}. \tag{B.1}$$

In chapter 5 we consider estimating the power spectrum using the multiplicative and min processors, which requires the use of the S-2 normalization. For the same L-sensor ULA, we can obtain the true PSD estimates by normalizing the weight vector by its L2 norm, i.e.,

$$(\textbf{S-2}) \qquad \frac{\mathbf{w}}{||\mathbf{w}||_2} = \frac{\mathbf{w}}{\sqrt{\sum_{i=1}^{L} |\mathrm{w(i)}|^2}}. \tag{B.2}$$

When the subarrays of a multiplicative or min processor are normalized using the S-2 scheme the spectral density estimate at the output of the processors requires to be corrected for a bias. This is done to ensure that comparisons between the spectral estimates obtained from multiplicative, min and conventional beamformers, the spectral levels are consistent for error analysis (the error analysis is one of the suggested future directions for this research).

The bias correction factor for the multiplicative processor considering a S-2 based normalization scheme for two basic signal models:

- **Noise only:** when the input is white noise, the output of the multiplicative processor averaged over a number of snapshots K can be given as,

$$E[|y_K|] = \sigma_n^2 \underbrace{\frac{\left|\sum_{i=shared} \mathrm{w}_A^*(i)\mathrm{w}_B(i)\right|}{||\mathbf{w}_\mathrm{A}||_2||\mathbf{w}_\mathrm{B}||_2}}_{=\beta} = \sigma_n^2\beta. \tag{B.3}$$

The output power received using the ULA does not require normalization. The output power obtained using the product processor needs to overcome the bias issue by dividing the averaged spectrum by β.

- **1 source:** The signal model chosen here makes use of one source at direction u_1 with signal power σ_1^2. The peak power of the source signal using the conventional processor normalized for PSD can be predicted to be,

$$|y_{ula}(u_1)|^2 = \sigma_1^2\left(\frac{\sum \mathbf{w}}{||\mathbf{w}||_2}\right)^2. \tag{B.4}$$

Similarly, the CSA response at the peak of the source signal can be predicted by,

$$|y(u_1)| = \sigma_1^2\left(\frac{\sum \mathbf{w}_\mathrm{A}}{||\mathbf{w}_\mathrm{A}||_2} \times \frac{\sum \mathbf{w}_\mathrm{B}}{||\mathbf{w}_\mathrm{B}||_2}\right). \tag{B.5}$$

We propose correcting for the bias using the factor ζ, which is defined as,

$$\begin{aligned}\zeta &= \frac{\left(\frac{\sum \mathbf{w}}{||\mathbf{w}||_2}\right)^2}{\frac{\sum \mathbf{w}_\mathrm{A}}{||\mathbf{w}_\mathrm{A}||_2} \times \frac{\sum \mathbf{w}_\mathrm{B}}{||\mathbf{w}_\mathrm{B}||_2}}, \\ &= \left(\frac{\sum \mathbf{w}}{||\mathbf{w}||_2}\right)^2 \times \frac{||\mathbf{w}_\mathrm{A}||_2}{\sum \mathbf{w}_\mathrm{A}} \times \frac{||\mathbf{w}_\mathrm{B}||_2}{\sum \mathbf{w}_\mathrm{B}}.\end{aligned} \tag{B.6}$$

Therefore, applying the constant ζ to the estimate of the output power obtained using the multiplicative processor provides with same peak level as predicted by the ULA,

$$\zeta \times |y(u_1)| = \sigma_1^2 \left(\frac{\sum \mathbf{w}}{||\mathbf{w}||_2} \right)^2 = |y_{ula}(u_1)|^2. \tag{B.7}$$

Similarly, for the min processor, Liu and Buck propose a bias correction factor (γ) when the two subarrays make use of the unity gain normalization (S-1) [44]. But when the subarrays are normalized for true PSD (S-2), the bias correction for the two cases discussed above,

- **Noise only:** No bias correction is required since both the subarrays provide with similar estimate of the noise power.
- **1 source:** The bias correction needs to be applied to each of the subarrays as it is processed independently, i.e.,

$$E[y_{min}(u_1)] = min(|\eta_A \times y_A(u_1)|^2, |\eta_B \times y_A(u_1)|^2). \tag{B.8}$$

Where,

$$\begin{aligned} \eta_A &= \frac{\sum \mathbf{w}}{||\mathbf{w}||_2} \times \frac{||\mathbf{w}_\mathrm{A}||_2}{\sum \mathbf{w}_\mathrm{A}}, \\ \eta_B &= \frac{\sum \mathbf{w}}{||\mathbf{w}||_2} \times \frac{||\mathbf{w}_\mathrm{B}||_2}{\sum \mathbf{w}_\mathrm{B}}. \end{aligned} \tag{B.9}$$

Bibliography

[1] H. L. Van Trees, *Optimum Array Processing (Detection, Estimation and Modulation Theory, part IV)*. John Wiley & Sons Inc, 2004.

[2] D. H. Johnson and D. E. Dudgeon, *Array signal processing: concepts and techniques*. Simon & Schuster, 1992.

[3] A. V. Oppenheim and R. W. Schafer, *Discrete-time signal processing*. Pearson Education India, 1999.

[4] S. Haykin, "Array signal processing," *Englewood Cliffs, NJ, Prentice-Hall, Inc., 1985, 493 p. For individual items see A85-43961 to A85-43963.*, vol. 1, 1985.

[5] D. King, R. Packard, and R. Thomas, "Unequally-spaced, broad-band antenna arrays," *IRE Transactions on Antennas and Propagation*, vol. 8, no. 4, pp. 380–384, 1960.

[6] A. Ishimaru, "Theory of unequally-spaced arrays," *IRE Transactions on Antennas and Propagation*, vol. 10, no. 6, pp. 691–702, 1962.

[7] A. Maffett, "Array factors with nonuniform spacing parameter," *IRE Transactions on Antennas and Propagation*, vol. 10, no. 2, pp. 131–136, 1962.

[8] R. Harrington, "Sidelobe reduction by nonuniform element spacing," *IRE Transactions on Antennas and Propagation*, vol. 9, no. 2, pp. 187–192, 1961.

[9] X. Zhu and J. R. Buck, "Designing nonuniform linear arrays to maximize mutual information for bearing estimation a," *The Journal of the Acoustical Society of America*, vol. 128, no. 5, pp. 2926–2939, 2010.

[10] H. Unz, "Linear arrays with arbitrarily distributed elements," *IRE Transactions on Antennas and Propagation*, vol. 8, no. 2, pp. 222–223, 1960.

[11] A. Moffet, "Minimum-redundancy linear arrays," *IEEE Transactions on antennas and propagation*, vol. 16, no. 2, pp. 172–175, 1968.

[12] D. Pearson, S. U. Pillai, and Y. Lee, "An algorithm for near-optimal placement of sensor elements," *IEEE Transactions on Information Theory*, vol. 36, no. 6, pp. 1280–1284, 1990.

[13] C.-Y. Chen and P. P. Vaidyanathan, "Minimum redundancy mimo radars," in *Circuits and Systems, 2008. ISCAS 2008. IEEE International Symposium on*. IEEE, 2008, pp. 45–48.

[14] M. Ryle, "A new radio interferometer and its application to the observation of weak radio stars," in *Proceedings of the Royal Society of London A: Mathematical, Physical and Engineering Sciences*, vol. 211, no. 1106. The Royal Society, 1952, pp. 351–375.

[15] A. Covington and N. Broten, "An interferometer for radio astronomy with a single-lobed radiation pattern," *IRE Transactions on Antennas and Propagation*, vol. 5, no. 3, pp. 247–255, 1957.

[16] E. Shaw and D. Davies, "Theoretical and experimental studies of the resolution performance of multiplicative and additive aerial arrays," *Radio and Electronic Engineer*, vol. 28, no. 4, pp. 279–292, 1964.

[17] D. Davies and C. Ward, "Low sidelobe patterns from thinned arrays using multiplicative processing," in *IEE Proceedings F (Communications, Radar and Signal Processing)*, vol. 127, no. 1. IET, 1980, pp. 9–15.

[18] A. Ksienski, "Multiplicative processing antenna systems for radar applications," *Radio and Electronic Engineer*, vol. 29, no. 1, pp. 53–67, 1965.

[19] M. Pedinoff and A. Ksienski, "Multiple target response of data-processing antennas," *IRE Transactions on Antennas and Propagation*, vol. 10, no. 2, pp. 112–126, 1962.

[20] D. Davies, "High data rate radars incorporating arrays signal processing and thinned arrays," in *International Radar Conference*, 1975, pp. 371–375.

[21] P. P. Vaidyanathan and P. Pal, "Sparse sensing with co-prime samplers and arrays," *IEEE Transactions on Signal Processing*, vol. 59, no. 2, pp. 573–586, 2011.

[22] P. Pal and P. Vaidyanathan, "Nested arrays: A novel approach to array processing with enhanced degrees of freedom," *IEEE Transactions on Signal Processing*, vol. 58, no. 8, pp. 4167–4181, 2010.

[23] K. Adhikari, J. R. Buck, and K. E. Wage, "Extending coprime sensor arrays to achieve the peak side lobe height of a full uniform linear array," *EURASIP Journal on Advances in Signal Processing*, vol. 2014, no. 1, 2014.

[24] Y. Liu, J. R. Buck, and R. Bautista, "Spatial power spectral estimation using coprime sensor array with the min processor," *The Journal of the Acoustical Society of America*, vol. 139, no. 4, pp. 2109–2110, 2016.

[25] D. F. Gingras, "North Elba sea trial summary," 1994.

[26] D. H. Johnson and P. N. Shami, "The signal processing information base," *IEEE Signal Processing Magazine*, vol. 10, no. 4, pp. 36–42, 1993. [Online]. Available: http://spib.linse.ufsc.br/sonar.html

[27] D. F. Gingras and P. Gerstoft, "Global inversion of acoustic field data in shallow water using genetic algorithms," in *Full field inversion methods in ocean and seismo-acoustics*. Springer, 1995, pp. 317–322.

[28] J. L. Krolik, "Robust matched-field beamforming with benchmark shallow-water acoustic array data," in *1996 IEEE International Conference on Acoustics, Speech, and Signal Processing*, vol. 2, 1996, pp. 1185–1188.

[29] J. Tabrikian, J. Krolik, and H. Messer, "Robust maximum-likelihood source localization in an uncertain shallow-water waveguide," *The Journal of the Acoustical Society of America*, vol. 101, no. 1, pp. 241–249, 1997.

[30] J. L. Krolik, "The performance of matched-field beamformers with Mediterranean vertical array data," *IEEE Transactions on Signal Processing*, vol. 44, no. 10, pp. 2605–2611, 1996.

[31] P. Welch, "The use of fast fourier transform for the estimation of power spectra: a method based on time averaging over short, modified periodograms," *IEEE Transactions on audio and electroacoustics*, vol. 15, no. 2, pp. 70–73, 1967.

[32] G. Heinzel, A. Rüdiger, and R. Schilling, "Spectrum and spectral density estimation by the discrete fourier transform (dft), including a comprehensive list of window functions and some new at-top windows," *Retrieved from http://hdl.handle.net/11858/00-001M-0000-0013-557A-5*, 2002.

[33] F. J. Harris, "On the use of windows for harmonic analysis with the discrete fourier transform," *Proceedings of the IEEE*, vol. 66, no. 1, pp. 51–83, 1978.

[34] B. Maranda, "Efficient digital beamforming in the frequency domain," *The Journal of the Acoustical Society of America*, vol. 86, no. 5, pp. 1813–1819, 1989.

[35] K. Adhikari, J. R. Buck, and K. E. Wage, "Beamforming with extended co-prime sensor arrays," in *Acoustics, Speech and Signal Processing (ICASSP), 2013 IEEE International Conference on*. IEEE, 2013, pp. 4183–4186.

[36] V. Chavali, K. E. Wage, and J. R. Buck, "Coprime processing for the Elba island sonar data set," in *Signals, Systems and Computers, 2014 48th Asilomar Conference on*. IEEE, 2014, pp. 1864–1868.

[37] F. B. Jensen, W. A. Kuperman, M. B. Porter, and H. Schmidt, *Computational ocean acoustics*. Springer Science & Business Media, 2000.

[38] K. Adhikari and J. R. Buck, "Gaussian signal detection by coprime sensor arrays," in *Acoustics, Speech and Signal Processing (ICASSP), 2015 IEEE International Conference on*. IEEE, 2015, pp. 2379–2383.

[39] M. K. Simon, *Probability distributions involving Gaussian random variables: A handbook for engineers and scientists*. Springer Science & Business Media, 2007.

[40] N. O'Donoughue and J. M. Moura, "On the product of independent complex gaussians," *IEEE Transactions on signal Processing*, vol. 60, no. 3, pp. 1050–1063, 2012.

[41] L. C. Stange, C. Metz, and A. F. Jacob, "Reducing cross-target products in thinned antenna arrays using nonlinear processing," in *Microwave Conference, 2002. 32nd European*. IEEE, 2002, pp. 1–4.

[42] M. B. Porter, "The kraken normal mode program," DTIC Document, Tech. Rep., 1992.

[43] I. Stakgold and M. J. Holst, *Green's functions and boundary value problems.* John Wiley & Sons, 2011, vol. 99.

[44] Y. Liu and J. R. Buck, "Detecting gaussian signals in the presence of interferers using the coprime sensor arrays with the min processor," in *Signals, Systems and Computers, 2015 49th Asilomar Conference on.* IEEE, 2015, pp. 370–374.

Curriculum Vitae

Vaibhav Chavali graduated from Atomic Energy Junior College, Mumbai, Maharashtra, in 2008. He received his Bachelor in Engineering from University of Mumbai in 2012. He is currently enrolled for a Master of Science degree in Electrical Engineering at George Mason University.